



Full length article

Martensitic twin boundary migration as a source of irreversible slip in shape memory alloys

Ahmed Sameer Khan Mohammed, Huseyin Sehitoglu*

Department of Mechanical Science and Engineering, University of Illinois at Urbana-Champaign, 1206W Green St., Urbana, IL 61801, United States



ARTICLE INFO

Article History:

Received 31 May 2019

Revised 15 November 2019

Accepted 21 December 2019

Available online 31 December 2019

Keywords:

Interface structure

NiTi

Shape Memory Alloys

Slip emission

Twin boundary migration

ABSTRACT

The mechanistic origin of fatigue in Shape Memory Alloys (SMAs) is addressed using atomistic simulations. A causal explanation is proposed for the known agreement between the fatigue-activated slip system and the martensitic twinning system. As a model system, the Type II twin boundary (TB) in NiTi B19' martensite phase is analyzed. TEM-based models have established the presence of disconnections on the TB. Topological models establish the TB migration to depend on the motion of twinning partials on these disconnections. A disconnection is setup within a Molecular Statics (MS) framework. A twinning partial is positioned on it by enforcing continuum displacement fields external to a prescribed core of atoms which is subsequently relaxed under governance of the interatomic potential. The displacement fields are calculated from the anisotropic Eshelby-Stroh formalism and enforced in a non-Cauchy-Born adherent manner to obtain the right core structure. TB migration is simulated as a motion of this disconnection under applied load. In the presence of a barrier to this motion, a dislocation reaction occurs where a stacking fault emits at the TB while returning a residual negated partial. The emissary fault partial is proposed as a precursor to the resulting slip observed in reverse-transformed austenite.

© 2020 Acta Materialia Inc. Published by Elsevier Ltd. All rights reserved.

1. Introduction

SMAs form a special class of materials that can handle large strains (several percent) and exhibit exceptional strain-recoverability owing to a diffusionless martensitic transformation [1]. When their microstructures are engineered to have load orientations favoring transformation over plasticity [2], they offer the exciting solution of handling large reversible strains under fatigue loading, possibly evading plasticity-induced fatigue damage dominant in conventional metallic materials [3,4]. Such reversibility is enhanced when the critical slip stresses of the individual phases (austenite and martensite) are higher than the critical stress for transformation. Considerable research in the field of SMAs is directed at further separating the two stress levels [5,6]. Nevertheless, these materials are not immune to fatigue damage mechanisms, and are subject to irreversible plastic slip activity, typically observed to accumulate in the austenite phase [7–15]. The manifestations of such mechanisms have two fronts, one is structural fatigue damage as observed in conventional metallic materials while the other is functional fatigue where shape memory performance characteristics such as recoverable strain, stress hysteresis etc. are significantly diminished [14,16–21]. In turn, the prevalence of such damage mechanisms negatively impacts applications of

SMAs in all domains, spanning biomedical (stents, orthodontics), automotive (valves) and aerospace fields [22].

One of the most puzzling aspects of SMA fatigue is the occurrence of plastic slip accumulation at stress levels far lower than the plastic flow stresses of the individual phases [5]. In fact, even stress-free thermal cycling of SMAs exhibit increasing dislocation density [13,23]. A continuum micromechanical approach to the problem may state that the higher local stress state at the interface, necessary to accommodate lattice and constitutive mismatch, can drive plastic slip. However, without a dislocation source, the stress levels must approach those of the ideal shear slip strength of the phases and this is unlikely. This is supported by the high unstable stacking fault energy barrier in the Generalized Stacking Fault Energy (GSFE) curves of the austenitic phase, particularly in those slip systems which have been shown to prevail under fatigue loading [24]. Further, several studies over the past few decades have consistently shown that the fatigue-activated slip system emanates from the austenite–martensite interface. Also, the slip system was found to align with the internal twinning system of martensite. In other words, the direction of Burgers vector of the emitted slip dislocation and the corresponding slip plane match the direction of twinning shear and twinning plane within the martensite phase, respectively (Fig. 1) [12,13,23]. These arguments lead us to believe that there is indeed a dislocation mechanism that is active at nominal stress levels (at the transformation stress) and is closely tied to the internal twinning within martensite.

* Corresponding author.

E-mail address: huseyin@illinois.edu (H. Sehitoglu).

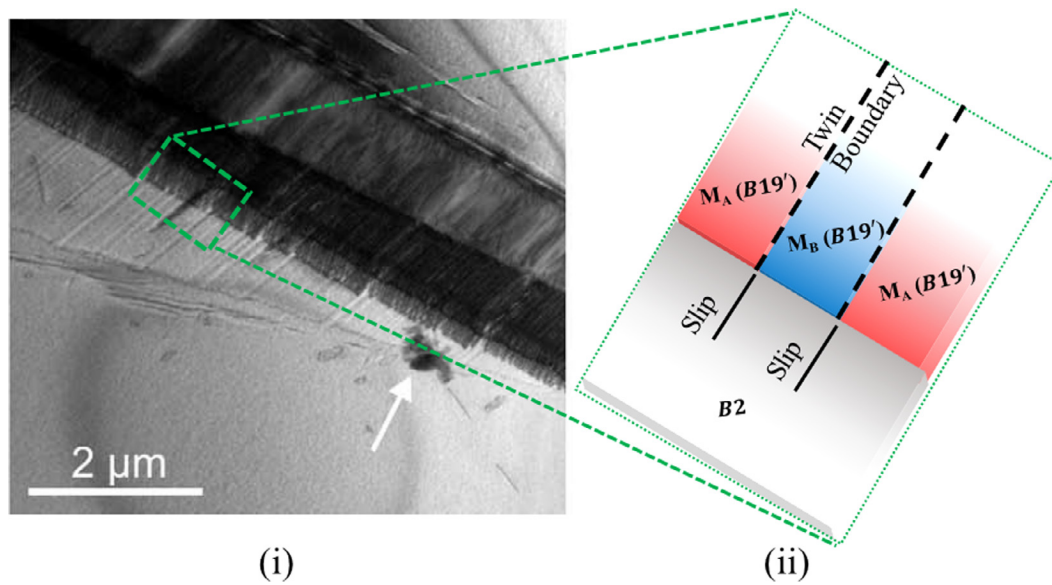


Fig. 1. (i) This TEM micrograph was captured *in situ* during the reverse transformation from martensite to austenite. The micrograph shows a receding martensite phase (dark colored needle) which is subdivided into very fine twins, and the austenite phase (lighter color matrix) exhibiting fine slip lines aligned with the internal subdividing twin boundaries of the martensite phase; image was taken from [13], the arrow points out a reference feature in the sample utilized for TEM imaging (ii) An accompanying schematic for clarification (labelled phases are specific to NiTi, for this study); the emitted slip line in the austenite B2 phase aligns with the twinning system in the martensite B19' phase.

To the best of the author's knowledge, only one proposition of a candidate dislocation reaction exists in literature and it involves a build-up of twinning partials on the martensitic TB [7,8]. While this mechanism proved a key step toward conceptual understanding of slip-emission during transformations, few pressing issues remain that could not be addressed due to the limitations of available tools at the time. The source of the participating twin partials is unclear. Even if the presence of such partials is presumed and a dislocation reaction follows, the accommodation of the residual dislocation within the participating TB must be addressed. The core atomic movements that underlie the reaction are unknown. Finally, the energetic feasibility of the dislocation reaction requires justification. An elementary energy-balance of the reactant and product dislocations (following Frank's rule) would render it infeasible. What is not accounted for is the energy influx due to a build-up of one or more twinning partials against a barrier to TB motion. In Kajiwara's scheme [8], the barrier is provided at the austenite-martensite phase due to the high resistance to slip in the austenite phase on the slip system aligned with the internal twinning. This explanation is based on the knowledge of accepted slip systems of the austenitic phase and lacks further quantification.

Multiple developments over the past two decades allow us to address aforementioned issues and examine the problem with exceptional detail that not only clarify mechanistic intricacies but also elicit key physical parameters that quantify the viability of the mechanism. Topological Modeling has established the disconnection-dislocation model for interfaces that migrate in a diffusionless manner [25–30]. They have been applied to twin interfaces to explain TB migration [27,29,31], consolidating classically understood dislocation-mediated twin-growth mechanisms [32–35]. These models establish the association between a TB disconnection to the corresponding twinning dislocation or twinning partial. Given the presence of such disconnections on the TB (as found in the chosen study target), the presence of participating twinning partials is then known. The advent of atomistic simulation tools implementing Molecular Dynamics (MD) [36] and Density Functional Theory (DFT) [37] allow a first-principles rooted analysis of dislocation interactions. The physical fidelity of these simulations is ensured by development of reliable interatomic interaction potentials [38–40]. Simulations of this nature present a framework for a quantitative concerted exploration of energetics implicitly accounting for dislocation

self-energies, interaction energies, lattice friction characterized by Generalized Fault energies (GSFE and GPFs) [41,42] while capturing core atomic motion with adequate detail.

In the following study, equiatomic NiTi is chosen as the model shape memory material owing to its commercial success [43,44], and because many of its potential applications characteristically involve cyclic loading conditions [4]. For instance, functional fatigue of NiTi actuator springs and structural fatigue of NiTi wires, particularly in medical components negatively impact performance and has inspired active research in the field spanning the past two decades [45–49]. As noted before, an effective way of quantitatively understanding the mechanism is by way of atomistic simulation. For this purpose, a MS approach is chosen by running energy minimization routines in LAMMPS under appropriate boundary conditions. The choice was governed by the need to simulate dislocation mechanisms at a scale higher than those involving *ab-initio* DFT calculations. Also, the distinction of MS over Molecular Dynamics (MD) is key here because the energy minimization allows a framework based solely on the potential energy of the atomic arrangements and is unperturbed by statistical kinetic effects associated with finite temperature dynamics. The chosen interatomic potential [40] was proven to consistently reproduce the right formation energies and elastic constants of both austenite and martensite phases. The ability to simulate shape memory and superelastic effects was demonstrated [50], and further it can structurally reproduce shuffled atomic positions characteristic of the phase. The importance of such shuffles will find relevance throughout the study. Nevertheless, it must be emphasized that since the potential is not fitted to slip or twin energy signatures which are the GSFE and GPFs respectively, the capacity to reproduce such features is indeed an open question. However, the fact remains that no potential for NiTi has been developed to account for all these phenomena [38–40,51–55]. In fact, developing potentials for such complex systems is still an active area of research and by no means is it reasonable to expect an empirical potential to be fit to all possible structural parameters. However, the present approach does not demand accuracy to quantitatively reproduce the energy signatures. It is known that different atomic configurations will correspond to highs and lows on the potential energy landscape and the potential is only required to capture these differences in a relative sense. It will be shown that the chosen potential has sufficient physical fidelity for this purpose.

Since the internal twinning in martensite consistently correlates with the fatigue-activated slip system in many SMAs, the TB in B19' is chosen as the system under scrutiny. The (011) type II system is favored owing to its common occurrence experimentally [44,56]. The HRTEM imaging of the boundary [57,58] was a breakthrough in understanding the structure of the TB. A key finding was the direct observation of a disconnected geometry for the TB, explaining the irrational $\sim(0.7205 \ 1 \ \bar{1})$ indices to result from stepping between consecutive $(1 \ 1 \ \bar{1})$ rational terrace planes. Consequently, it implies that twinning partials reside on these disconnections [27,29,35], and could participate in a slip-emission mechanism, similar to that of [8]. Surprisingly, only one study thus far has established the magnitude of this partial, obtained from the periodicity of the twin-migration region in the Generalized Planar Fault Energy (GPFE) curve [59]. It also provides sufficient insight into the detwinning mechanism useful for this study. Understanding this mechanism is vital to know the core atomic motions involved during twin partial motion and subsequently understand the consequence when a barrier is presented to it.

In summary, the dislocation mechanism proposed by Kajiwara [8] is examined quantitatively for the NiTi SMA within a MS framework. For this purpose, the type II twinning system of B19' is studied. Following the atomic models in [57–59], coherent twin segments are setup with a twinning-partial on a disconnection in between the segments. Under an applied shear strain, twin partial motion and subsequent build-up against a barrier is enforced and a candidate dislocation reaction is simulated and proposed as a possible irreversibility active during fatigue (refer Fig. 2). The current study is but the starting step in analyzing fatigue-induced irreversibilities in SMAs. It is intended to subsequently steer toward physics-based fatigue modeling (similar to [60]) in SMAs, by providing characteristic structural parameters instrumental in relevant dislocation mechanisms.

2. Methodology

A brief outline of the approach will be presented. Given the crystallography and the atomic models provided in [57–59], coherent twin “segments” are constructed within a MS framework. In each twin variant, the atomic sites are color-coded differently to aid visual identification of the detwinning mechanism. The rationale for this choice will be evident later in the study. Each twin “segment” corresponds to the TB structure on the {111} terraces (excluding the disconnections). To

ensure that this structure is in a stable configuration, a MS energy minimization is carried out for each twin segment. Multiple segments with the TB on successive {111} planes are assembled to set-up a disconnected twin geometry in the simulation box. In order to locate the twin partial dislocations at the disconnections, an indirect approach is employed where continuum displacement fields of the dislocation are enforced outside a central core, and the core allowed to relax under their constrained positions, at the mercy of the chosen interatomic potential. This method is often used to obtain the right atomic arrangement at the core of the dislocation. The calculation of displacement fields at the interface between two highly anisotropic media (i.e. the martensite variants) is performed by employing the Eshelby-Stroh formalism [61], given the elastic constants of both phases and the magnitude of the twinning partial. A crucial catch in this procedure is in knowing how to apply the displacement fields around the core. It is not applied to all atoms but only to certain atoms, the choice of which is informed through a study of the detwinning mechanism. Once the displacement fields are enforced in accordance with the mechanism, the cores of the partials are in arrangements that ensure a twinned wake as they move. The entire system is carefully relaxed using MS. Finally, a displacement-controlled shear strain is applied to initiate motion of the partials and generate a build-up against an artificially enforced barrier. The build-up of a single twinning partial against a barrier is simulated, and the consequent dislocation reaction is reported with justification.

2.1. Coherent {111} twin segments

The unit cell parameters are chosen consistent with the interatomic potential [40]. The atomic sites in the unit cell are depicted in Fig. 3(i) where one of the Ti atoms is at the lattice point (0, 0, 0), following a commonly adopted crystal description [44,62]. This Ti atom shall henceforth be called a lattice Ti while the other Ti atom of the unit cell shall be called a motif Ti. Inverted color-coding of the lattice-motif Ti sites are employed for the variants as shown in the Fig. 3(i). This distinction will be instrumental in describing the atomic shuffles associated with the detwinning mechanism necessary for TB migration. Notice that the Ni atoms are not distinguished. Their shuffles are completely analogous to the Ti atom shuffles and another distinction adds unrequited complication in understanding the study.

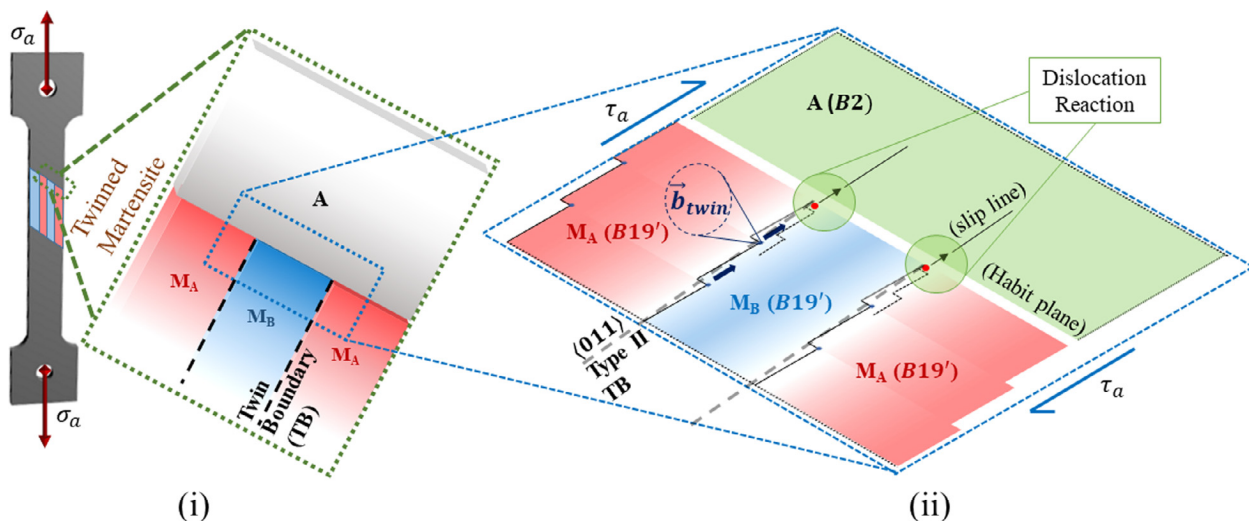


Fig. 2. (i) An SMA dog-bone specimen undergoing martensitic transformation (austenite phase, A, to martensite phase) under applied load; the martensite phase forms as a twinned structure with variants M_A and M_B , separated by the twin boundary (compare with Fig. 1) (ii) This schematic is specific to the system of interest i.e. NiTi (transformation from austenite B2 to B19' martensite phase), with the internal twin boundary as the (011) Type II TB; The TB is typically approximated as a straight irrational plane (dashed line) at higher scales, but at the nanoscale it has a disconnected geometry with rational {111} terrace planes (solid lines); The schematic depicts the motion of twinning partials on disconnections and a possible dislocation reaction emitting slip into austenite (note the alignment of the slip line with the TB); the reaction occurs in the event the leading twin partial encounters a barrier (depicted as a red dot). (For interpretation of the references to colour in this figure legend, the reader is referred to the web version of this article.)

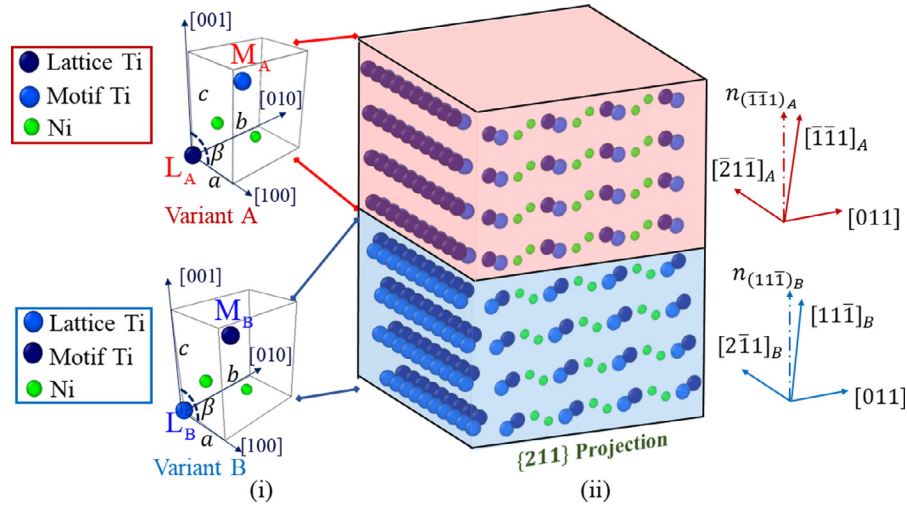


Fig. 3. (i) Labelling of atomic sites in the unit cell of NiTi B19' martensite; notice the lattice (L)-motif (M) Ti labeling distinct for each variant (ii) A 3-dimensional view of Coherent {111} twin segment relaxed within MS (the frontal {211} projection is shown along with a lateral view of the 3D structure only showing the Ti atoms, utility of which is realized ahead in visualizing twin partial motion); the crystallography used for construction of the atomic structure is given adjacently.

As mentioned earlier, a twin “segment” will be used to refer to the part of the type II TB between consecutive disconnections. Henceforth, the variant on top of the twin interface shall be labelled A (colored red) while that on the bottom shall be labelled B (blue). The interface between the variants is rational and coherent [63]. The atomic model of the variants are constructed following the crystallography elaborated in [59], and assembled to form the twin segment (Fig. 3(ii)). Nonetheless, construction of this twinned configuration is not trivial and requires accounting of interface coherence strains and a lattice offset between the variants. Since this study is focused on proposing a candidate dislocation reaction, a digression into these details is avoided here and the reader is directed to Appendix B for a better exposition. The resulting structure is relaxed within MS to ensure that the configuration is stable as governed by the interatomic potential. The simulation box axes are aligned as $x \parallel [011]$, $y \parallel [2\bar{1}\bar{1}]_A$, $z \parallel n_{\{111\}}$. Periodic conditions can be applied along x and y because these directions are crystallographic, thereby approximating the bulk of the material parallel to the plane of the coherent terrace. Due to the monoclinic distortion of B19' martensite, the z direction is not crystallographic and periodic conditions cannot be enforced. Instead, shrink-wrapped conditions are employed with a $6A^0$ thick layer “frozen” in place on the top and bottom. These atoms are presumed to be sufficiently far from the TB within the bulk of each variant to remain unaffected by the local interface structure. The size of the layer is chosen to be higher than the potential's cut-off ($r_c = 5.2\text{\AA}$) [40]. The box size is chosen to be approximately $63.6 \times 82.9 \times 125.8A^3$, which is 10 times the periodic spacing in both $x \parallel [011]$ and $y \parallel [211]$ directions, and 60 {111} planes stacked along the normal to the twin interface.

The structure is relaxed under the conjugate gradient energy minimization scheme in LAMMPS [36], whose fractional energy tolerance for convergence is set at 1.0×10^{-8} . The simulation box size is kept constant throughout. Fig. 3(ii) represents the relaxed atomic structure of the twin segment. These twin segments will be instrumental in setting up a TB disconnection, in Section 2.3.

2.2. Locating twin-partials in an atomistic framework

An accepted approach to positioning a dislocation within a discrete atomic structure (in a Molecular Statics or Dynamics framework) involves enforcing atomic displacements corresponding to the continuum field solution of the dislocation. All atoms beyond a specified core radius from the dislocation line are displaced in accordance to those fields and constrained while the mobile core is allowed to relax, governed by the interatomic potential [64]. The purpose of the enforced displacement fields is

to prepare the atomic configuration in a manner from which a constrained minimization by the potential leads to the right core structure. Nevertheless, the first step is to solve for the continuum displacement fields. The linear elastic anisotropic Eshelby-Stroh formalism is adopted for this purpose, where the relevant equations and their results are presented in the following section. Subsequently, the application of these displacement fields within an atomistic framework is discussed.

2.2.1. Continuum displacement fields of the twin partials

In the anisotropic Eshelby-Stroh formalism for an interface dislocation, the displacement fields are described by a set of complex constants, solved for each of the two phases sharing the interface. Constants corresponding to the twinning variant A shall be indicated with a superscript A, while those for variant B shall be indicated by a superscript B. The coordinate system is defined by the triad of vectors $\vec{t} - \vec{m} - \vec{n}$, where the normal $\vec{n} = [0\ 0\ 1]$ points from phase B to A, $\vec{t} = [1\ 0\ 0]$ corresponds to the dislocation line vector parallel to [011], and $\vec{m} = [0\ 1\ 0]$ points away from the dislocated half-plane ($x_2 < 0$). In this system, the burger's vector is given by $\vec{b} = 1/9[011]_M \approx [0.7066\ 0\ 0]A^0$. The displacement fields $u_i (i = 1, 2, 3)$ for the two domains are given by:

$$u_i^A(\mathbf{x}) = \frac{1}{2\pi\sqrt{-1}} \sum_{\alpha=1}^6 A_{i\alpha}^A E_{\alpha}^A \ln(\mathbf{m} \cdot \mathbf{x} + p_{\alpha}^A \mathbf{n} \cdot \mathbf{x}) \quad (\mathbf{n} \cdot \mathbf{x} > 0) \quad (1)$$

$$u_i^B(\mathbf{x}) = \frac{1}{2\pi\sqrt{-1}} \sum_{\alpha=1}^6 A_{i\alpha}^B E_{\alpha}^B \ln(\mathbf{m} \cdot \mathbf{x} + p_{\alpha}^B \mathbf{n} \cdot \mathbf{x}) \quad (\mathbf{n} \cdot \mathbf{x} < 0) \quad (2)$$

The constants $(p_{\alpha}, A_{i\alpha})$, $(\alpha = 1, 2, \dots, 6)$ for each domain is obtained by solving the equilibrium condition for the stress-field. For instance, the equilibrium condition in the variant A gives us:

$$\sigma_{ij,j}^A = C_{ijkl}^A u_{k,lj}^A = 0 \quad (3)$$

For a non-trivial solution, this leads to a set of algebraic equations,

$$C_{ijkm}^A (\mathbf{m}_i + p_{\alpha}^A \mathbf{n}_i) (\mathbf{m}_m + p_{\alpha}^A \mathbf{n}_m) A_{k\alpha}^A = 0 \quad (4)$$

And for a non-trivial $(p_{\alpha}^A, A_{i\alpha}^A)$, the following condition ensues:

$$\det\{C_{ijkm}^A (\mathbf{m}_i + p_{\alpha}^A \mathbf{n}_i) (\mathbf{m}_m + p_{\alpha}^A \mathbf{n}_m)\} = 0 \quad (5)$$

And for every p_{α}^A , there exists a vector a values for $A_{k\alpha}^A (k = 1, 2, 3)$ from Eq. (4). The constants E_{α} for each phase is obtained by solving

conditions that relate tractions and displacements across the slip plane. For the half-plane given by $x_2 < 0$, the displacements and tractions are both continuous, yielding the following equations respectively

$$\sum_{\alpha=1}^6 A_{i\alpha}^A E_{\alpha}^A - \sum_{\alpha=1}^6 A_{i\alpha}^B E_{\alpha}^B = 0 \quad (i = 1, 2, 3) \quad (6)$$

$$\sum_{\alpha=1}^6 L_{i\alpha}^A E_{\alpha}^A - \sum_{\alpha=1}^6 L_{i\alpha}^B E_{\alpha}^B = 0 \quad (i = 1, 2, 3) \quad (7)$$

For the half-plane $x_2 > 0$, the Burgers vector represents the discontinuity across the slip plane, resulting in the following displacement and traction conditions respectively:

$$\sum_{\alpha=1}^6 \eta A_{i\alpha}^A E_{\alpha}^A + \sum_{\alpha=1}^6 \eta A_{i\alpha}^B E_{\alpha}^B = 2b_i \quad (i = 1, 2, 3) \quad (8)$$

$$\sum_{\alpha=1}^6 \eta L_{i\alpha}^A E_{\alpha}^A + \sum_{\alpha=1}^6 \eta L_{i\alpha}^B E_{\alpha}^B = 0 \quad (i = 1, 2, 3) \quad (9)$$

In these equations, the expression for $L_{i\alpha}$ in each phase is given by the following example for variant A:

$$L_{i\alpha}^A = -n_j C_{ijkm}^A (m_m + p_{\alpha}^B n_m) A_{k\alpha}^A \quad (10)$$

The elastic constants are picked consistent to those reproducible by the interatomic potential [40]. The constants are given in Table 1. Due to twin symmetry, $p_{\alpha}^A = p_{\alpha}^B = p_{\alpha}$.

The twin-partial is of screw nature and the displacement component parallel to the dislocation line (the major component) is shown in Fig. 4 (ii). To aid visualization, an accompanying schematic representation is shown in Fig. 4(i). Now, the continuum displacement solution is available for superposition to individual atoms in the MS simulation.

2.2.2. Applying displacement fields: non Cauchy-Born adherence

In MS or MD, the primary focus is to setup a physically consistent dislocation core that can move under an applied load, and in the event of dislocation reactions, present atomic configurations that can interact to form product dislocations. Both features find relevance in this study. A crucial assumption implicit in the procedure is the Cauchy-Born (CB) assumption whereby all atoms outside the core are assumed to adhere to the continuum displacement fields. An argument is made in the following section as to why it may not lead to the right core structure in B19' owing to the presence of shuffles.

As mentioned earlier, the enforced displacement fields provide a surrounding constraint that guides the MS relaxation. The goal is to relax the sharp displacement gradient of the continuum solution to a smoother physically consistent atomic-scale disregistry at the dislocation core. By nature of the twin-partial, it resides on a TB disconnection [27,29] and the core-structure transitions the atomic arrangement from that in one variant to the other variant across the disconnection. Within the core, the nature of disregistry (as the structure transitions) has a one-one correspondence to the interface disregistries encountered in atomistic simulation of the GPFE curve (refer Appendix D). The role of continuum displacement fields in conditioning the core structure is exactly analogous to the role of

rigid displacements in the GPFE calculation used to enforce local disregistry at the twin interface.

For high-symmetry systems such as cubic structures (FCC, BCC etc.), the disregistries are dominantly translational and do not involve shuffle of any significant proportion. For this reason, the GPFE displacements can be applied to all atoms to achieve the detwinning (Appendix D). This relates with the enforcement of continuum displacement fields on all atoms surrounding the dislocation core, and the Cauchy-Born assumption prevails. This is the case in several atomistic studies involving dislocations, where the assumption is often tacit [65–70]. In the case of B19', detwinning requires disregistries of both a translational and shuffle character. There is a lattice-motif Ti shuffle and also a shuffle of Ni atoms. To achieve the detwinning in the GPFE, the displacements must only be enforced on specific Ti sites while the remaining atoms shuffle about their positions. This is addressed in more detail in Appendix D. The major takeaway being that the continuum displacement fields must be applied more selectively around the core, and the Cauchy-Born assumption is not followed.

Surmising the detwinning mechanism in as much is relevant to this section: The lattice-motif Ti shuffles occur along [011] while the Ni shuffles occur perpendicular to this direction (refer Appendix C). The displacement field is then applied to select Ti sites in both variants whose detwinning atomic motions align with the direction of the displacement field at that location. In variant A, these correspond to lattice Ti sites while in variant B they correspond to motif Ti sites. This is illustrated in Fig. 4 (iii).

The following section addresses the construction of the TB disconnection upon which the twin partials are positioned in the manner described above.

2.3. Construction of TB disconnection and twin-partial core structure

To construct a TB disconnection, coherent twin segments that were independently relaxed (Section 2.1) are assembled piecewise. The choice of the number of disconnections in the simulation box indirectly decides the number of participating twinning partials for the simulated dislocation reaction. It must be reiterated, that no knowledge of such a dislocation reaction is yet available in literature. There is only a hypothesis that it could relate to twin-partial build-up but the number of reacting partials, and the outcome of such a reaction have not been established conclusively. To that extent, the approach presented here is exploratory, does not force a specific reaction, and only sets conditions conducive for it. A disconnected TB is setup with one disconnection and a twin partial located on that disconnection.

Lateral periodicity is preferred to mimic conditions closer to a bulk material, and to avoid boundary effects (or any unwanted image force resistance to dislocations) during simulation of the reaction. Ideally, it would be preferred to orient the effective twinning plane $\{0.7205 \bar{1}\bar{1}\}$ aligned with the xy plane of the simulation box and enforce periodicity. However, the effective plane is not a crystallographic one and will cause issues when implemented with periodicity. For this reason, the coherent terrace of the TB i.e. the $\{1 \ 1 \ \bar{1}\}$ plane is preferred instead. And to include disconnections with twinning partials, a mirrored ledge structure is constructed as shown in Fig. 5(i). A large span is chosen for the central ledge to allow one half of the simulation box to mimic the physical TB and the twin-partial interaction.

At each disconnection, the displacement fields are enforced as outlined in Section 2.2.2 and the atoms are relaxed to produce the right core structure. The relaxation refers to the energy minimization using the conjugate gradient scheme with the same tolerance as in Section 2.1. Physically, this guides the core of the twinning partial to a state where there is a gradation of shuffled positions. This is illustrated in Fig. 5(ii) and 5 (iii), by visualizing the atomic positions at the core of the twin partial, on the slip plane, and the transition in Ti-shuffles is observed along (211). The right core structure renders the required mobility for the twinning partials under applied load, while

Table 1
Eshelby-Stroh Constants for Twin-partial of (011) Type II twin.

p_1	$-0.3273+1.3438i$	E_1^A	$-0.2204+0.0154i$	E_1^B	$0.2204-0.0154i$
p_2	$-0.3091+0.9710i$	E_2^A	$0.3171-0.0462i$	E_2^B	$0.3171-0.0462i$
p_3	$0.2313+0.7117i$	E_3^A	$0.0848+0.0174i$	E_3^B	$-0.0848-0.0174i$
p_4	$-0.3273-1.3438i$	E_4^A	$0.2204+0.0154i$	E_4^B	$-0.2204-0.0154i$
p_5	$-0.3091-0.9710i$	E_5^A	$-0.3171-0.0462i$	E_5^B	$-0.3171-0.0462i$
p_6	$0.2312-0.7117i$	E_6^A	$-0.0848+0.0174i$	E_6^B	$0.0848-0.0174i$

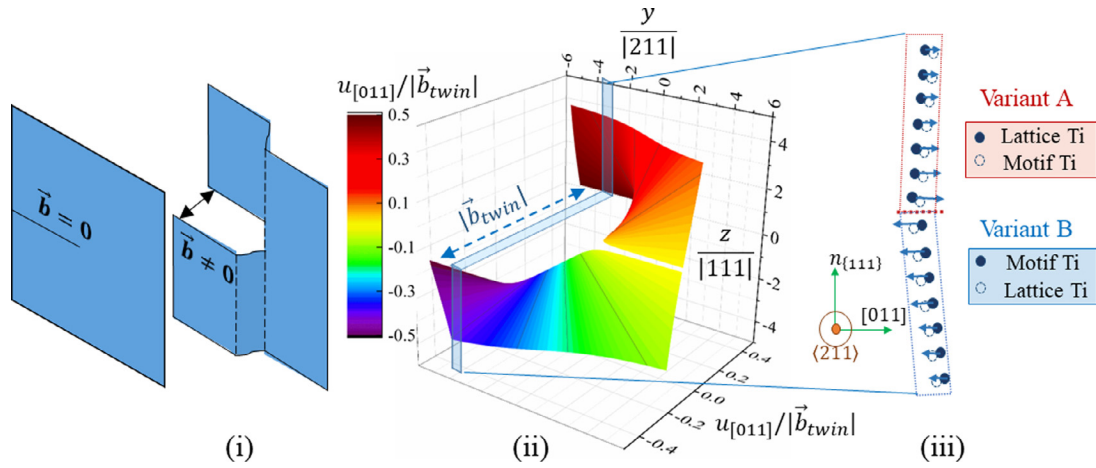


Fig. 4. (i) Schematic representation of displacement discontinuity introduced by a screw dislocation, included to aid visualization of displacement field (ii) Major component of the displacement field solved from the Eshelby-Stroh formalism; the Burgers vector is shown, and a 2D displacement profile is sectioned (iii) Superposition of the 2D displacement profile onto a representative column of atoms on the $\{211\}$ plane; the displacement fields are applied selectively to certain Ti sites in both variants, indicated by the coloring schema.

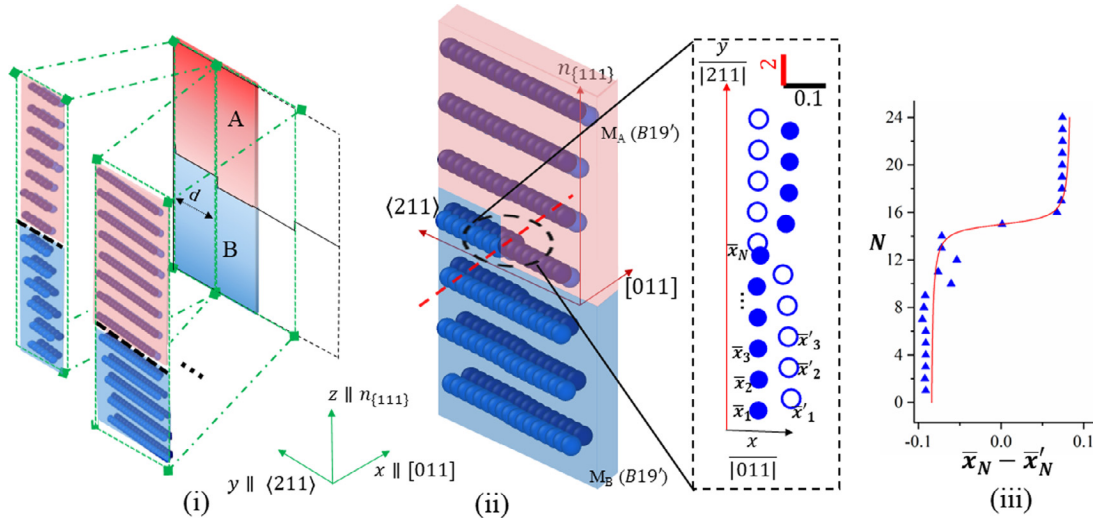


Fig. 5. (i) Construction of MS Simulation setup for dislocation reaction, indicating the mirrored ledge construction of twin interface (assembled piecewise from independently relaxed $\{111\}$ twin segments) (ii) Relaxed atomic configuration around a TB disconnection, after introduction of the displacement fields on specific Ti sites (only the Ti atoms are shown for brevity and as mentioned in text, coloring schema of variant B is reversed to emphasize the shuffle across variants) (iii) After identifying corresponding lattice and motif sites, the transition in shuffled states at the core of the twin-partial (represented through a scaled schematic and plot) is visualized; \bar{x}_N and \bar{x}'_N respectively represent normalized $[011]$ coordinates of lattice and motif Ti atoms, and the shuffles are quantified by $(\bar{x}_N - \bar{x}'_N)$ where N is a simple count of the lattice-motif pairs tracked across the disconnection.

ensuring that the all-important detwinning mechanism is followed as it propagates on its plane.

2.4. Final simulation: setup of dislocation reaction within MS

So far, only the atomic configuration suitable for the final simulation of the dislocation reaction has been setup. Now a displacement-controlled shear loading is enforced to move the twinning-partial (Fig. 6(ii)). Subsequently, a barrier is presented to the motion of this partial and the outcome of that interaction is observed. The procedure for setting up these conditions will be elaborated.

Following the boundary conditions of section (2.1), lateral periodic conditions are enforced and shrink-wrapped conditions applied parallel to the TB. A constrained layer with thickness larger than the potential's cut-off radius is chosen at the top and bottom of the simulation box. The constrained layers parallel to the TB serve to provide rigid atomic blocks at the boundaries which can be moved to enforce a strain-controlled deformation within the box. Note that in this setup, the twinning partial is a screw partial (Burgers vector parallel

to dislocation line). The partial is moved by applying a shear on the simulation box by incrementally displacing the top and bottom frozen layers. The top is moved in the positive x direction (along $[011]$) while the bottom layer in the negative x direction, thereby enforcing a xz shear conducive to motion of the screw partial on the TB, along $\langle 211 \rangle$. At each incremental displacement of the boundary, the simulation box is relaxed under the same parameters of (2.1). In this manner, a strain-controlled shear load is applied within the framework of molecular statics. No kinetic energy is involved, and the configuration is allowed to find the minimum energy positions at every strain increment, ensuring a “quasi-static” condition as best as it can be expected within atomistic simulation frameworks. Note that since there is no dynamics in this system, this applied loading is not coupled with high strain-rates which is often the caveat in such simulations, furnishing more reasonable stress estimates.

Thus, the simulated mechanical stress-strain response focuses on manifestation of intrinsic potential energy barriers and hence captures the athermal response. Although sufficient for the purposes of the present work, it is prudent here to mention relevance to physical experiments where one is necessarily in the regime of finite temperatures

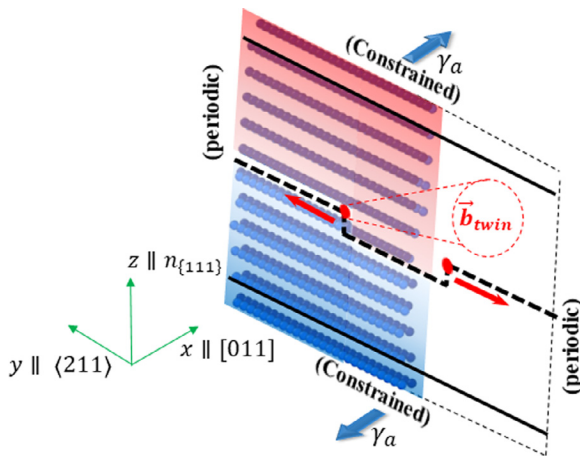


Fig. 6. Final Simulation setup: Under constrained/periodic boundary conditions, motion of twin partials on disconnections is simulated under applied shear (a dislocation dipole is constructed, a positive twin partial is positioned on the left-side disconnection and a negative twin-partial on the right-side disconnection).

(say ambient temperature ~ 300 K) and finite strain-rates (for instance 10^{-3}s^{-1}). In such conditions, the structure is assisted by additional thermal energy to overcome the energy barrier, governed by statistical thermodynamics. Consequently, the stress level required to activate the sought dislocation mechanism (to occur at a rate that is significant in comparison to the applied strain-rate) would be lower than that predicted by the present athermal approach. Nonetheless, results of the present work could, in principle, be extended to this scenario by interpreting the determined athermal energy barriers as an activation energy in an Arrhenian expression. This is better elaborated in texts concerning thermally activated deformation, a good exposition for which can be found in [71].

Under applied shear, the twin-partial moves and migrates the TB. This migration is achieved by motion of the disconnections, progressively converting atoms in variant B configuration to that of variant A (refer Fig. 6). To generate a build-up a barrier needs to be provided ahead of the leading partial. The question now becomes: how is the barrier/stop enforced? The answer lies in knowing the detwinning mechanism (refer Appendix C). Since, the twin partial essentially shuffles the Ti and Ni positions, a stop can be introduced by preventing these shuffles explicitly. An explicit prevention of lattice-motif Ti shuffles at a certain location ahead of the leading partial was implemented. When the leading partial reaches this juncture, it cannot

progress further because shuffle is disallowed. Implementing the barrier is not trivial. For a small group of atoms at the barrier location, forces in the direction of shuffle were selectively ignored during the relaxation. Nevertheless, these atoms were allowed to follow the applied shear motion by imposing displacements equal to the average of displacements experienced by surrounding atoms. Now that a twin-partial motion is setup and a barrier enforced, dislocation reactions are set-up by creating a build-up of one twin-partial against the barrier. Visualization is done using Open Visualization Tool (OVITO) [72] where snapshots at incremental shear strains are recorded. The results will be discussed in the following section.

3. Simulation results on twin partial slipping and barrier interaction

When no barrier is imposed to the motion of the twin partial, the partial slips across the coherent terrace, and reaches the lateral boundaries of the simulation box. A few snapshots of a focused subset of atoms are shown in Fig. 7, labelled with the average shear strain on the simulation box at that instant. At a certain critical shear stress, the shuffle-reliant detwinning mechanism activates and advances the partial, and the partial continues to the boundary. The advancement of the shuffle is visualized more closely, emphasizing the importance of the core structure elaborated in Section 2.3. The benefit of the choice in color coding of atomic sites (Section 2.1) is now realized as the shuffles are visualized in the exchange in the position of the dark-blue and light-blue spheres, representative of the lattice-motif Ti shuffles (Appendix C).

When a barrier is imposed to the shuffle (in the manner explained in Section 2.4), the partial halts at that position, and the applied shear builds up. Eventually, a dislocation reaction seems to occur at the TB. The most conspicuous change is that the direction of advancement of the shuffle is reversed, progressing in a direction opposite to that associated with the original twin partial. Thus, along the TB, the original progression of detwinning has reversed, now converting atoms in variant A arrangement to that of variant B. This indicates that a negative twin partial has nucleated which under the action of the applied shear moves in the opposite direction, achieving such a detwinning effect. In the onward direction, there seems to be a formation of a stacking fault at the TB. In other words, given that the shuffle has been disallowed, a translational disregistry has nucleated at the barrier and has progressed forward. And interestingly, it does not form within either of the variants but rather nucleates at the TB between them. Intuitively, this is an agreement with the twin symmetry of the structure as there is no special preference given to either of the variants. The relevant snapshots of

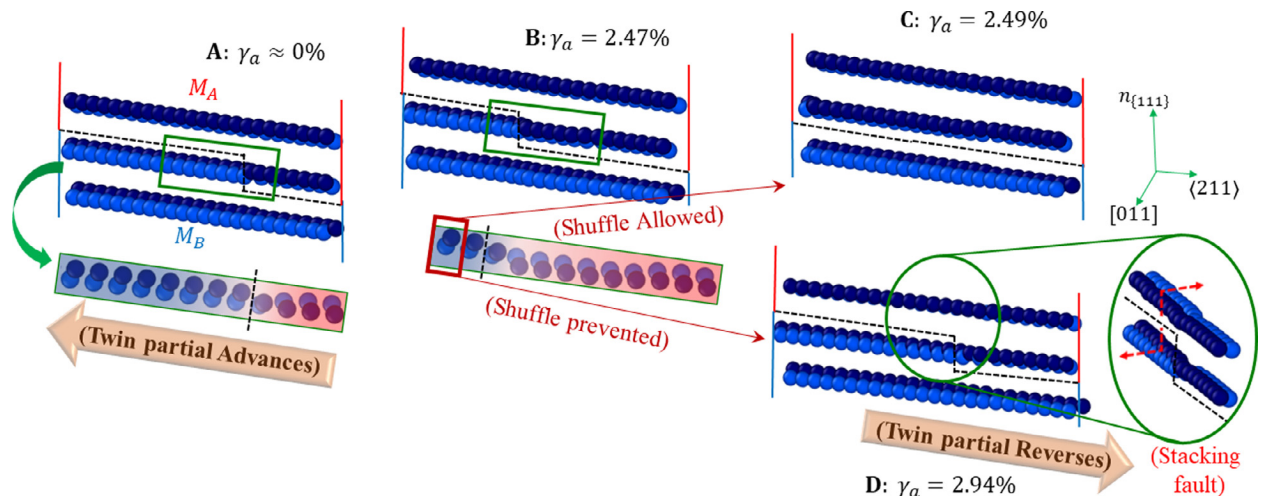


Fig. 7. Snapshots of dislocation reaction simulation depicting twin partial advancement and reversal in the presence of a shuffle barrier (bordered red). (For interpretation of the references to colour in this figure legend, the reader is referred to the web version of this article.)

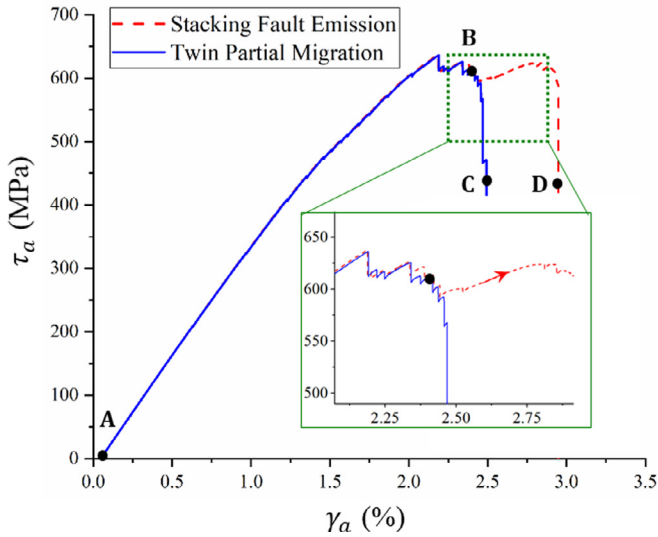


Fig. 8. Stress-Strain response in the event of twin partial migration and fault emission; the inset reflects the additional hardening in the presence of a shuffle barrier.

the sequence are shown in Fig. 7. Analogous to the shuffle-progression, a snapshot showing the core atomic motions are visualized, for the fault nucleation. For a better illustration, short animation videos corresponding to both cases have been provided as supplementary material. At this stage, the hypothesis for fault nucleation is more argumentative and a more thorough analysis will be presented subsequently.

The stress-strain curves for both cases are shown in Fig. 8. The twin-partial motion can be inferred from the stress-plateau in both scenarios. When a barrier is present, there is an additional hardening regime to a slightly higher stress-level at which the fault partial is hypothesized to nucleate and slip. Notice that the stress-level for fault nucleation is close to that corresponding to the onset of twin-partial motion.

A Region of Interest (ROI) is defined in the path of the migrating twin partial, ahead of the shuffle barrier. Thus, the ROI is positioned close to the extremity of the (211) edge of the simulation box (shown in Fig. 9(i)). It is defined as a thin cuboidal region, with the longest edge along the z axis of the simulation box. It is used to query certain averaged properties of the atoms contained within the region. Hence the ROI only acts as a measuring probe during the simulation. Two parameters, relative displacement and energy density (per unit area), are calculated from it. The relative displacement is taken as the average displacement of variant A contained within the ROI minus that of variant B within the same region. The ROI is chosen to be small along [011] and (211) to resolve local changes due to motion of the partial. The choice of the parameters is motivated from the state variables that are typically reported in GPFE/GSFE calculations (planar energy and relative displacement). The dimensions of the ROI are approximately $\sim |011| \times |211| \times z_{\max}$, which is one periodic spacing in the x and y directions and spanning the entire simulation box normal to the TB. A larger span was chosen along z to capture far-field average displacement discontinuities introduced by sweeping of a dislocation through the ROI. If the z dimension is chosen to be smaller, then the average displacements are marred by the twinning shuffles anti-parallel to the applied shear (refer Appendix C), and a representative trend is not observed. The difference of average displacement between atoms in the top and bottom twin variants within the ROI is recorded along with the total energy which is normalized against $A_{ROI} \sim |011| \times |211|$. The energy at zero shear strain is taken as the reference datum. The results are shown in Fig. 9 (iii, iv).

There is a sharp discontinuity in displacement (denote as $[u]$) and the energy (denote as $[E]$) in both cases, which is expected when any dislocation sweeps through the ROI. The magnitudes of the displacement jump

$[u]$ do not exactly match the dislocation magnitude because of averaging over displacement gradients within the finite span of the ROI. Nonetheless, they correlate with the dislocation magnitudes and will only be used as a relative measure in this context. It was observed that only the $\langle 011 \rangle$ displacement (aligned with the applied shear) component exhibits appreciable change while the relative displacements in the other directions are minor (lower by at least one order of magnitude) and shall be ignored. During twin partial motion, the discontinuous jump in displacement (normalized) is approximately $[u]_{\text{twin}} \approx 0.025$. Note that there is a shuffle that occurs within the ROI as the partial sweeps through, and the average displacement difference within the ROI is considered here. The energy jump $[E]_{\text{twin}} \approx 55 \text{ mJ/m}^2$ also reasonably corresponds with the unstable energy barrier γ_{ut} in the GPFE (in Appendix D). When a barrier is presented and the twin-partial arrests, the first observation is that there is still a displacement jump within the ROI, implying that a dislocation (partial or full) has swept through. The jump is delayed in both the displacement and energy curves, occurring at a higher applied shear strain than in the former case. Note that the magnitude of the displacement jump is nearly twice that of the twinning partial, $[u]_{\text{fault}} \approx 0.045$. Still $[u] < |011|$, implying that it cannot be a full dislocation but is a leading partial of a fault within the TB. The energy barrier to be crossed before emission of said fault is higher than in the twinning case by $\approx 10 \text{ mJ/m}^2$, while the energy jump $[E]_{\text{fault}} \approx 40 \text{ mJ/m}^2$ is smaller.

Visualizing the changes in the ROI, it is observed that there is a translational disregistry corresponding to the observed displacement discontinuity, and there is no shuffle. Analogous to the previous case, the displacement jump is treated as a measure of the Burgers vector magnitude associated with the fault's leading partial. The emitted partial has a Burgers vector magnitude nearly twice of the twinning partial. This estimate shall be consolidated in the next section. Recall, it was argued before that there is a residual twinning partial of a negative sense emitted in the reverse direction away from the barrier. These observations agree with the crystallographic conservation laws governing dislocation reactions. In summary, the authors hypothesize the prevalence of the following dislocation reaction at the barrier:



This is schematically shown in Fig. 10. A single twin partial participates in the reaction. The reaction is dissociative in nature and does not occur spontaneously, as will be discussed in the following section. It requires a build-up against a barrier to the detwinning mechanism hindering motion of the participating twin partial.

4. Discussion of simulation results

4.1. Generalized stacking fault energies

Based on the observed atomic motions, a candidate reaction has been proposed. The nature of the emitted partial has been established as having a character of translational disregistry rather than a shuffle. It leads a fault that forms at the TB and has a Burgers vector aligned with the twinning partials, along [011] and no other components. The magnitude was assigned on the grounds of the displacement jump measured in the ROI and is also consistent with the conservation of Burgers vector, given the participating and residual twinning partials involved in the reaction. To make this more conclusive, a GSFE calculation is carried out at the TB. A rigid relative displacement is introduced between the two variants in the [011] direction, while allowing the atoms to relax (minor atomic motions) in the $\langle 211 \rangle$ and $n_{\{111\}}$ directions. The objective is to determine if there is a local minimum at a relative displacement matching the estimated Burgers vector, explaining the formation of the fault and its corresponding leading partial. The results are shown in Fig. 11. As expected, an energy minimum corresponding to a stable fault exists at the expected magnitude of the Burgers vector $u/|011| \approx 2/9$. Notice that

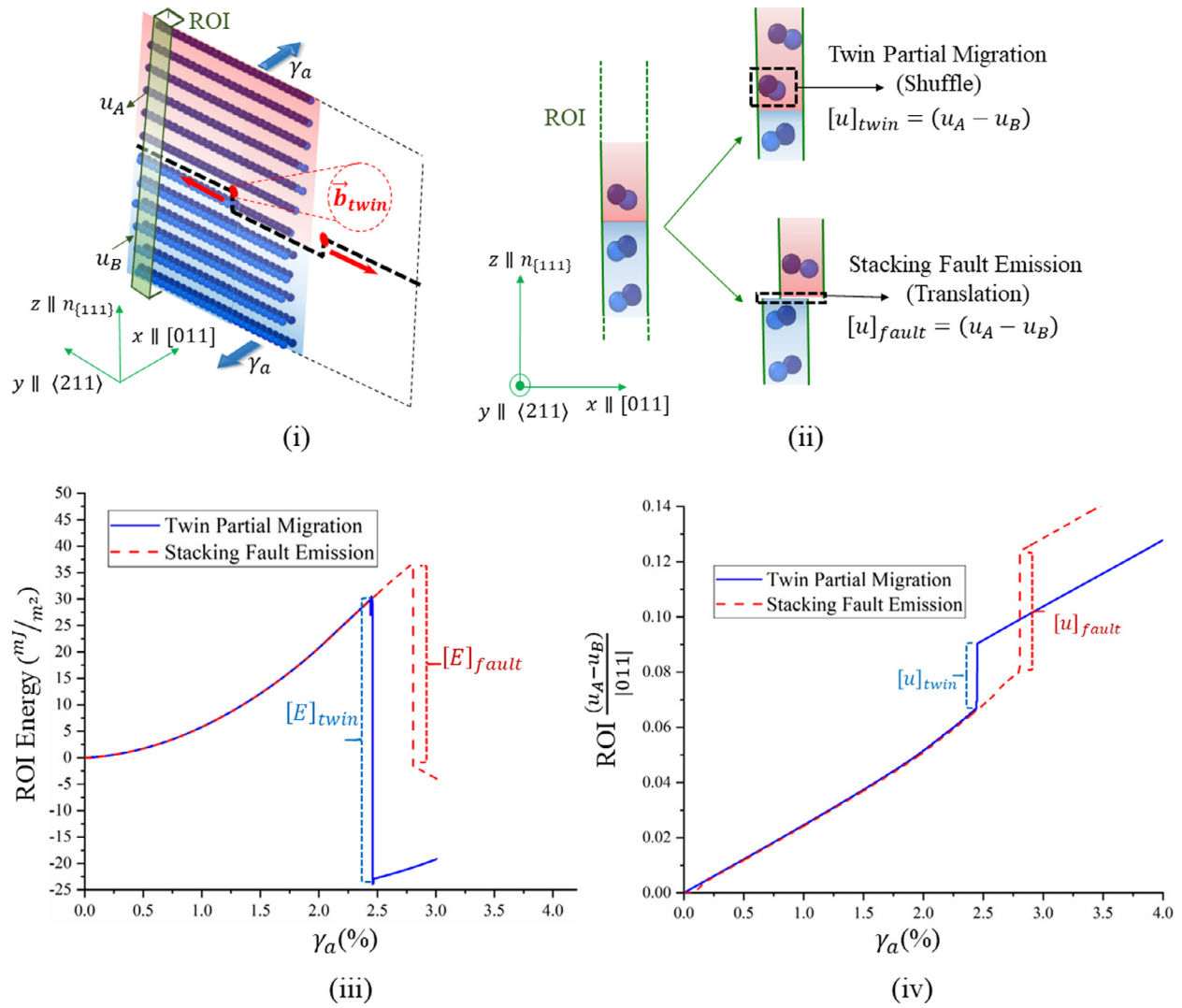


Fig. 9. (i) Region of Interest (ROI) to capture relative displacements and energy changes (ii) Snapshots of the central region within the ROI, emphasizing the difference in displacement jumps due to twin partial motion and stacking fault emission (iii) Energy change of ROI, emphasizing jumps $[E]$ (iv) Relative displacement within ROI, emphasizing jumps $[u]$ associated with dislocation motion; note that the jump associated with stacking fault emission is higher than for motion of the twinning partial.

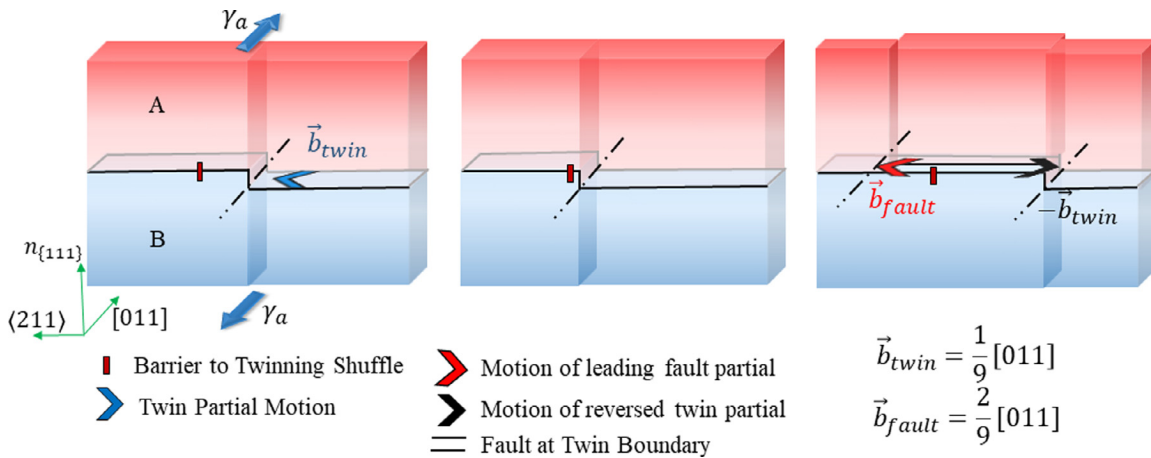


Fig. 10. Schematic of the proposed dislocation reaction at the shuffle barrier; From left to right, the twin partial moves under applied shear, stops at the barrier and dissociates into a leading fault partial and a retreating negated twin partial.

the magnitude of the corresponding unstable stacking fault energy barrier, γ_{us}^{twin} is only slightly higher than γ_{ut} , the difference being $(\gamma_{us}^{twin} - \gamma_{ut}) \approx 10mJ/m^2$. Also, the energy drop following this peak

γ_{us}^{twin} to the fault position is $\approx 45mJ/m^2$ reasonably close to the energy jump $[E]_{fault}$ determined before. Hence, these values are consistent with the difference in energy barriers and displacement jumps

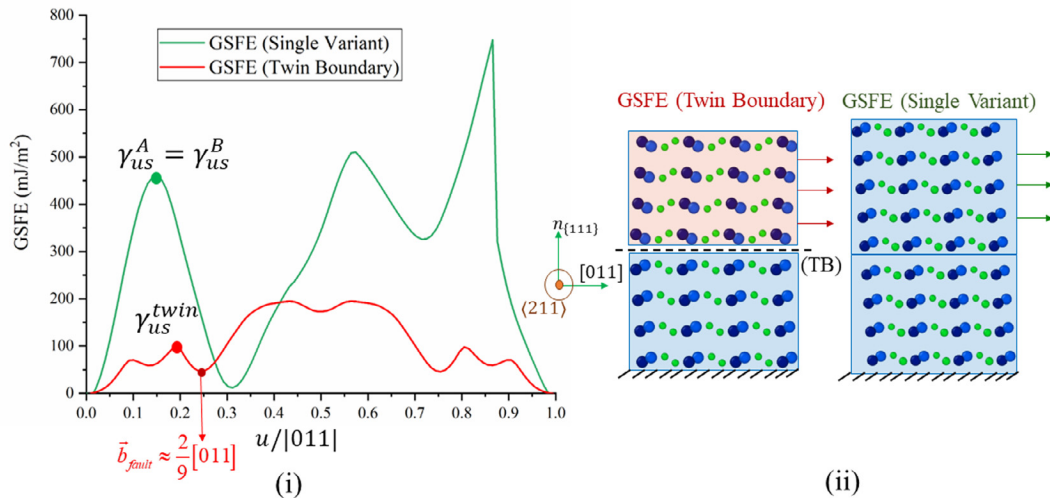


Fig. 11. (i) Generalized Stacking Fault Energy (GSFE) curves within a single martensitic variant, and across the TB, reflecting the slip resistance at both positions (the minimum corresponding to the fault partial is indicated) (ii) Schematic showing the procedure to calculate the GSFE curves for both cases.

crossed within the ROI, shown in Fig. 9. This correspondence confirms the nature of the fault and the corresponding Burgers vector of the stacking fault partial that is emitted. Note that although there is a preceding energy minimum at $u/|011| \approx 0.13$, it is not a candidate for the emitted fault partial because the residual Burgers vector that would remain after its emission would neither correspond to a negated twin partial, nor any other interface dislocation for the structure. Also, the corresponding energy signatures for this position (unstable fault barrier and the following energy drop) do not match the calculations at the ROI. Hence, the emitted fault partial is $\vec{b}_{fault} = 2/9[011]$.

The residual twin partial that is emitted in the reverse direction also resides on a disconnection. Despite an attractive elastic interaction with the twinning partial on the next successive plane, it wouldn't annihilate with the partial because there is an increasing energy cost associated with the reducing generalized planar fault length between successive twin partials. This energy cost is associated with the impending formation of an unstable 2-layer fault smaller than the stable nucleus for the type II twin in B19' martensite [59]. This is schematically illustrated in Fig. 12. Eventually, it is proposed that the solitary residual partial along with the rest of the twinning partials on the plane, does not perturb the spacing of disconnections by that much thereby maintaining the effective twinning plane to be nearly the same.

In order to justify that the formation of the fault at the TB, and not within any of the individual variants, a GSFE calculation is repeated within a variant. The results are shown in Fig. 11. The unstable fault energy barrier $\gamma_{us}^A (= \gamma_{us}^B)$ is significantly higher and no minimum is observed at the expected Burgers vector magnitude. This confirms that the emitted fault resides within the TB, and not within any of the variants.

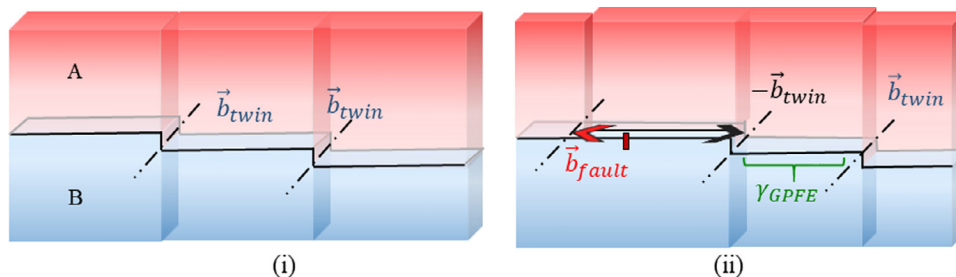


Fig. 12. A comparison of the twinning partial arrangement (i) before and (ii) after the dislocation reaction has occurred; the residual twinning partial does not annihilate with the next successive twin partial due to a repulsive component from increasing GPFE value.

4.2. Energetic feasibility of the proposed reaction

Now, a discussion on the energetics of the dislocation reaction will be addressed. An energy-balance based on Frank's rule makes it obvious that this reaction cannot happen spontaneously. Additional energy-input is required to drive the reaction. In the case of a single-partial, the additional energy is provided by the external load, as observed in the distinct hardening increment pointed out in Fig. 8. If there was no barrier, then the stress would have plateaued and done work sufficient to counter the lattice friction for detwinning. However, the fault emission requires a higher stress and corresponding energy influx which is manifested as a hardening in the stress-strain curve. In the case of NiTi, it is observed that the difference $(\gamma_{us}^{twin} - \gamma_{ut}) \approx 10 \text{ mJ/m}^2$ is very small and reflects as a minor hardening in the stress-strain curve before fault emission. This energy parameter quantifies the ease of occurrence of the reaction. Since the reaction is proposed as a source of irreversibility, the energy parameter is proposed as a characteristic physical measure of susceptibility to fatigue across different SMAs.

In this formulation employing a single twin partial, the supplementary energy influx for the reaction is furnished by the external shear. A brief argument outlining the role of elastic interaction between multiple twin-partial on the TB is prudent here. A schematic of the TB geometry is shown in Fig. 13(i) indicating the disconnection spacing. The continuum strain energy density per unit area of the TB is estimated against a parametric variation of the disconnection spacing. A representative volume element is chosen as shown in Fig. 13(ii). Since there is a twin symmetry, the energy partitioned between each of the variants is identical. Further, the periodic disconnection spacing provides a convenient cell size for the RVE. A large span is chosen normal to the direction of the TB. The strains, and

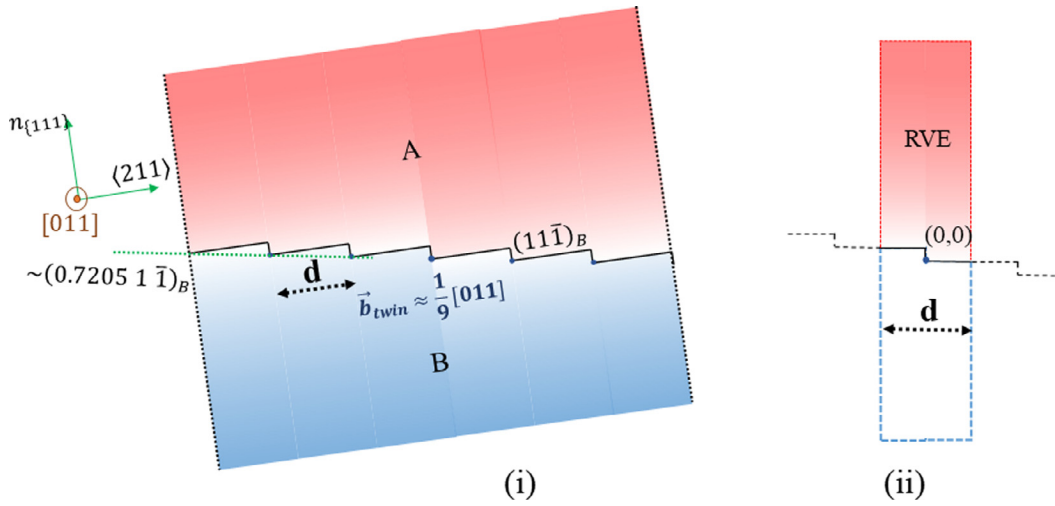


Fig. 13. (i) Schematic for the disconnected TB geometry (as suggested in [57]), indicating the $\{111\}$ terraces, the disconnections on which twin-partials reside and the effective plane $\{0.7205 \ 1 \ \bar{1}\}_B$ (figure adapted from [73]) (ii) RVE used to calculate the elastic energetics of the disconnected TB.

consequently the strain energy density, only vary in the yz plane (Fig. 6) and hence the energy estimate is normalized per unit length along x , and with the disconnection spacing in y , yielding a planar energy density per unit area of the TB.

The continuum elastic strain $\varepsilon_{partial}(y, z)$ surrounding an isolated partial are derived from the displacement fields calculated in Section 2.2.1. Within each RVE, the contribution of strain fields from $N_p = 50$ (needs to be sufficiently large) twin partials on either side are included to approximate the infinitely extending periodically spaced dislocation array on the TB. A crucial catch is that these strain fields are to be superposed over a coherence strain ε_{coh} (mentioned in Section 2.1 and elaborated in Appendix B) required for atomic registry at the interface. The strain energy density at each point within the RVE is calculated as,

$$\varepsilon(y, z) = \sum_{k=-N_p}^{N_p} \varepsilon_{partial}(y - kd, z + kh_{\{111\}}) + \varepsilon_{coh} \quad (12)$$

where $h_{\{111\}}$ is the normal distance between consecutive $\{111\}$ terraces, representing the step height at a disconnection. The planar energy density is calculated as an area integral over the RVE, normalized with the disconnection spacing:

$$E_{twin} = \frac{1}{d} \int_{RVE} \varepsilon^T(y, z) C_A \varepsilon(y, z) dS \quad (13)$$

The integration is done numerically because of the complex analytical forms of the displacement fields of the twin partial (Section 2.2.1). The energy density is plotted against the choice of disconnection spacing in Fig. 13(i). There is a competing effect between the dislocation array and the coherence strain. The least energy configuration corresponds to the state when the dislocation array relieves the coherence strain far away from the interface. This minima corresponds to the equilibrium spacing $d = 36.74 \text{ \AA}$, close to the predictions of [57,58]. At lower values, the energy is higher due to repulsive interaction between the dislocations. At higher spacing, the energy is higher due to the extended influence of the coherence strain further from the interface. Notice the asymmetry in the gradient of potential energy about the minimum point.

Fig. 14

One of the specialties of the Type II system is this behavior of the elastic interaction energy where a further separation of the interface dislocations can also incur a potential energy increase. Thus, any perturbation of the disconnection spacing, either as a build-up (reducing d) or

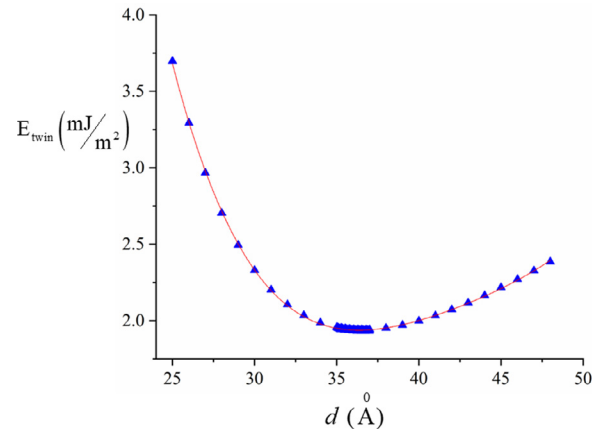


Fig. 14. Dependence of (011) Type II TB energy in NiTi on disconnection spacing.

a further separation (increasing d), can raise the potential energy and provide additional energy influx for the dislocation reaction. And while a theoretical argument for the role of build-up (reducing d) was provided in [74], the possible role of the latter behavior (increasing d) has not been studied.

The authors would like to mention that the interaction of multiple partials was also attempted within the same MS framework. However, the simulations were unstable, and often found disordered configurational minima. This is attributed to the limited capabilities of the chosen interatomic potential, unable to capture higher-scale micromechanics such as the interactions between partials. Nevertheless, given the repeatability of the observations associated with a single twin partial and supporting results/arguments explaining it, the physical fidelity of the simulated reaction is trusted and proposed as an active mechanism in this system. For an exact discourse on the role of twin-partial build-up, a more formal micromechanical study shall be undertaken as a future endeavor.

4.3. The source of irreversibility during transformation: slip emission

This phenomenon also has fundamental relevance to functional fatigue. The superelastic hysteresis of SMAs is associated with the motion of transformation dislocations within the twinned martensite and the austenite-martensite interface. The lattice frictional barrier

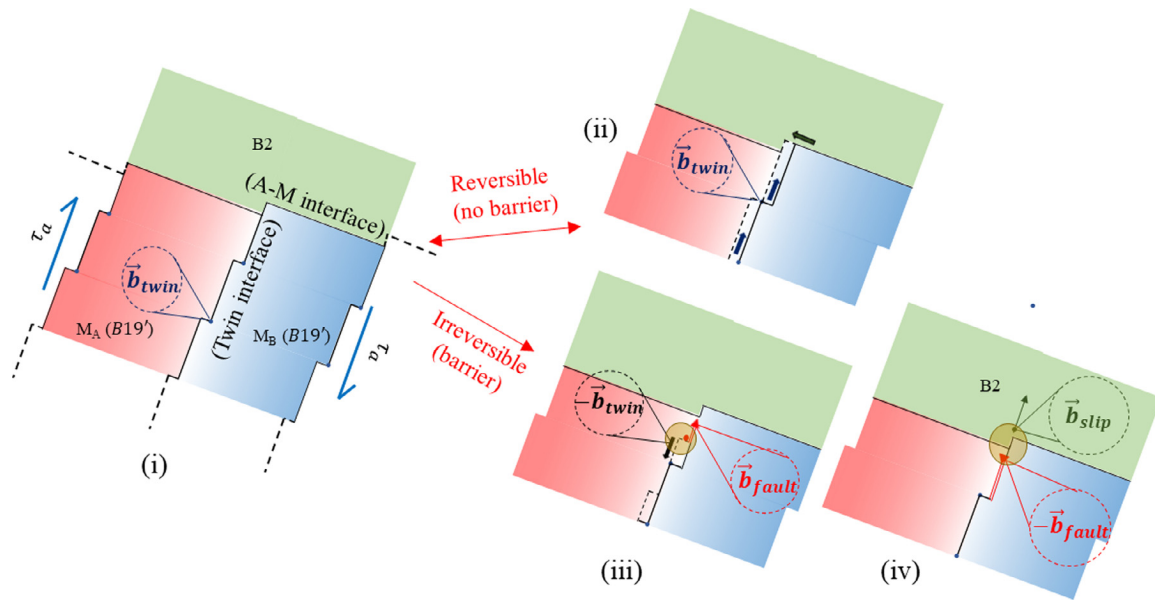


Fig. 15. (i) Topology of the martensitic twin interface and the Austenite-Martensite (A-M) interface (ii) Reversible twin partial migration to the A-M interface causing a disconnection advancement (iii) Dissociation of leading partial to form an advancing fault and a receding negated twin partial (analyzed and proposed by this study) (iv) Second dislocation reaction involving the leading fault partial and disconnection hypothesized to emit an austenitic slip dislocation while correcting the stacking fault.

that must be overcome by these dislocations during the forward and reverse transformation constitute the energy loss during superelastic cycling. Since the focus is on the TB within martensite, the motion of twinning partials shall be considered. In the absence of any of the aforementioned irreversibilities, the twinning partials move in the forward and reverse directions, migrating the TB reversibly. The energy dissipation corresponds to the area under the GPFE twin migration curve. In the presence of a barrier and the ensuing dislocation reaction, a higher lattice friction barrier must be overcome for the forward motion of the fault partial. This difference would correlate with the parameter $(\gamma_{us}^{twin} - \gamma_{ut})$, and fundamentally dictate the change in the recoverable hysteresis under superelastic cycling. Further, the emitted slip contributes to the irrecoverable strain that accumulates over multiple cycles.

All these implications arise out of the subtle distinction in structural evolution during twin-partial motion and interaction. It is in understanding this distinction, that the true potential of atomistic simulations has been realized. In the case without a barrier, the twin-partial migrates through a progression of shuffles while in face of a barrier, the progression switches to a translation disregistry, forming a fault at the TB. These have been visualized and clarified in Figs. 7, 9 and 10. This shuffle-translation dichotomy at the TB (refer Fig. 9(ii)), the associated Burgers vectors and the energy barriers form the crux of the reaction and its corresponding consequences to mechanical behavior.

The relevance of the proposed reaction in explaining the observed irreversible slip within austenite is explained. The emitted fault partial still resides within the twinned martensite but it is proposed as a precursor to a subsequent dislocation reaction that will emit a perfect dislocation into the austenite phase. In order to build an argument for this, a brief consideration of the morphology of the austenite-martensite (A-M) interface is necessitated. Multiple studies, based on topological modeling, have addressed the presence of transformation dislocations and disconnections on the A-M interface [26,30,75]. For the specific case of NiTi, this is still an open problem under study, particularly when it comes to clarifying

the meeting point of the twinned martensitic boundary with the A-M habit plane. Drawing from the topological models, a schematic is presented where the TB meets the A-M interface at a disconnection, shown in Fig. 15. When there is twin partial migration, it eventually meets the habit plane, and advances the disconnection as shown. Thereby the TB migration and habit-plane motion go hand-in-hand. In the presence of a barrier, and the subsequent occurrence of the proposed reaction, the partial is interrupted and a fault emitted. The residual twin partial of the reaction conserves the twin-boundary morphology in the wake, while the emitted fault disturbs it. As the leading fault partial approaches the disconnection, it is hypothesized that there must be a second reaction that occurs, which leads to an emission of a perfect dislocation in the austenite phase, and a residual partial $-b_{fault}$ which restores the fault back to the pristine TB. In contrast to the former case, without any barrier, the disconnection does not advance, but a dislocation is emitted into the austenite phase. Similar to the slip system of the fault partial, the emitted slip dislocation would also agree with the twinning system of martensite, thereby explaining several experimental results on fatigue of SMAs. Nevertheless, this idea, in its current form, is out of scope of the present study and is only proposed as a hypothesis to guide future studies in this direction.

In closing, few directions for further research are mentioned. The energetics of the dislocation reaction merits further attention. Apart from clarifying the feasibility of the reaction, it can allow calculation of critical stress levels for the reaction to occur. An estimate of how high this critical stress is, in comparison to the transformation stress levels, can quantify susceptibility to such dislocation irreversibilities. The significance of the energy influx from elastic interaction of multiple twin-partial (Section 4.2) must be considered. The energy barriers $(\gamma_{us}^A, \gamma_{ut}^{twin}, \gamma_{us}^{twin})$ proposed in this study will be vital atomistic inputs to calculate lattice friction stresses for the dislocations. An ab initio calculation using DFT can provide more reliable estimates for these energy barriers. While the scope of the present study was on one system in NiTi, the approach is more pervasive, providing a framework to analyze such reactions across different SMAs.

5. Conclusions

The present study focused on providing a causal explanation of fatigue-activated slip in NiTi SMA. Motivated by the consistent agreement of the slip system with the internal twinning system of martensite, the internal $\langle 011 \rangle$ Type II TB was analyzed. An exploratory study of possible dislocation reactions was undertaken within a framework of atomistic simulations (molecular statics), guided by an early mechanism proposed by Kajiwara [8]. The present study proposes the prevalence of a dislocation reaction during martensitic TB migration. The product dislocation is proposed to be a precursor to austenitic slip emission, so far understood only from an experimental standpoint. The following are the key contributions of this work:

- The core structure of the twinning partial was constructed by a non-Cauchy-Born enforcement of the continuum displacement fields around the core, within a MS framework. A gradation of shuffles was observed through the core, consistent with the mechanism of detwinning.
- The disconnected geometry of the TB was constructed within a MS framework, and the partials positioned at the disconnections. Under an applied shear, twin partial motion and subsequent build-up against a barrier was simulated. On the basis of simulation results, a dislocation reaction is proposed where the incoming twin partial dissociates to form a stacking fault on the TB ahead of the barrier. The leading partial of the fault has twice the magnitude of the incoming twin partial, and leaves behind a residual negated twin partial on a disconnection on the TB.
- The crux of this reaction lies in the dichotomy between twinning shuffles and translational fault disregistry at the twin-boundary. The latter is preferred when there is any barrier presented to the progression of shuffles. The additional energy influx could be aided by the build-up of twin partials against the barrier.

On the basis of the reaction, a physical parameter that can be used to characterize fatigue susceptibility of SMAs is proposed. The proposed reaction serves as a step toward understanding irreversible fatigue damage mechanisms in SMAs, from first principles. The goal is to lead toward a physics-based fatigue model, furnishing key material parameters that can profoundly affect fatigue behavior and hence real-world performance.

Declaration of competing interest

The authors declare that they have no known competing financial interests or personal relationships that could have appeared to influence the work reported in this paper.

Acknowledgements

The support of the Air Force Office of Scientific Research (AFOSR) under award number FA9550-18-1-0198, with Dr. Ali Sayir as Program Director, is gratefully acknowledged. This work made use of the Illinois Campus Cluster, a computing resource that is operated by the Illinois Campus Cluster Program (ICCP) in conjunction with the National Center for Supercomputing Applications (NCSA) and which is supported by funds from the University of Illinois at Urbana-Champaign.

Supplementary materials

Supplementary material associated with this article can be found in the online version at doi: [10.1016/j.actamat.2019.12.043](https://doi.org/10.1016/j.actamat.2019.12.043).

Appendix A. Terminology

This appendix provides brief explanations for some of the terms used specific to topological modeling and/or atomistic simulations. Appropriate references are provided for more detailed explanations.

Topological Modeling	An interface modeling approach used to model interfaces of diffusionless phase transformations (such as the martensitic transformation). This model proposes that such interfaces are not a single crystallographic plane but are “stepped”. The steps or “disconnections” separate crystallographic planes with non-zero interplanar distance between them. At the disconnection, interface dislocations are required to accommodate the lattice mismatch between the two phases. On the basis of symmetry relations and lattice mismatch strains between the constituent crystallographic phases, this model determines the spacing of the disconnections and the Burgers vector of the interface dislocation. These parameters together determine the interface structure [25,75]. Typically, such interfaces have irrational Miller indices (such as habit planes in SMAs). In this study, the $\langle 011 \rangle$ Type II twin boundary is such an interface.
Terrace	For a stepped interface, there exists a finite span of a crystallographic interface plane separating two consecutive steps. At this plane, the two phases are coherently bonded and the Miller indices of the plane are rational (represented in the crystallographic basis of either of the phases). This plane is called a “terrace” plane. In this study, the $\{111\}$ plane is a terrace plane for the Type II TB.
Disconnection	The “steps” between two consecutive terrace planes are called “disconnections”. The non-zero interplanar distance between two consecutive terraces is called the step-height, constituting one of the physical parameters associated with the disconnection. Another parameter associated with it is the Burgers vector of the dislocation that resides on it [27,29]. In this study, the step-height is equal to the spacing between consecutive $\{111\}$ planes. And the interface dislocation is the twinning partial.
GSFE (Generalized Stacking Fault Energy)	The GSFE represents the interatomic potential energy E_{GSFE} , associated with the introduction of a stacking fault between two consecutive crystallographic planes $\{hkl\}$. This is done by introducing an in-plane relative-displacement Δu (lmn) between the planes [76]. The GSFE is calculated using atomic-scale simulations, typically generating a 2D curve E_{GSFE} vs Δu . In this study, Fig. 11 plots GSFE curves and shows an accompanying schematic for clarification of the procedure. It can be used to calculate the athermal lattice-friction stress (also known as the critical slip stress) of a dislocation which has a slip system $\langle lmn \rangle \{hkl\}$ [77,78].
Unstable SFE barrier (γ_{us})	In simplest terms, it is a local maximum on the GSFE curve. This value quantifies the energy barrier for slip on the particular $\{hkl\}$ plane. In this study, we quantify the energy barrier for motion of the emissary fault partial using the corresponding unstable SFE value.
GPFE (Generalized Planar Fault Energy)	The GPFE is an extension of the GSFE used to calculate the interatomic potential energy E_{GPFE} , for nucleation and migration of a twin. Say the twinning system is given by the twinning plane $\{hkl\}$ and direction of twinning shear $\langle lmn \rangle$. Instead of introducing a single stacking fault between two planes, the GPFE calculation procedure introduces faults on multiple such plane-pairs to eventually generate a twinned structure from the parent phase [41,79]. A 2D curve is calculated as the energy versus the cumulative displacement associated with the introduction of the fault, E_{GPFE} vs Δu . It can be used to calculate critical twinning stresses [42,80], similar to how GSFE is used to calculate critical slip stresses.

(continued)

Twin Boundary (TB) Migration	The movement of the Twin Boundary (TB) in a direction normal to itself, by one crystallographic plane. By this process, it causes one twin variant to grow at the expense of the other.
Twin Migration segment of GPFE	The GPFE curve is generally partitioned into two segments – the twin nucleation segment and the twin migration segment. After the introduction of a certain planar fault length, the energy curve becomes periodic. From this point hence, a single period of the variation in energy is called the twin migration segment of the curve. The twin migration segment represents the energy to migrate the twin boundary by one additional plane [41].
Unstable Twin Migration Energy Barrier (γ_{ut})	It refers to the local maximum in the twin migration segment of the GPFE curve. It quantifies the energy barrier for the motion of the twinning partial. It is calculated in Appendix D for the Type II TB using Molecular Statics. A more accurate <i>ab initio</i> calculation can be found in [59].
Type II Twin	The classical theory of deformation twinning [81] establishes two distinct orientation relationships between the twin variants. The chosen system of interest follows the second orientation relationship, and hence is named Type II. In this mode, the twin variant lattices are related to each other by a 180° rotation. The twinning plane is irrational ($\sim \{0.72051\bar{1}\}$ in this case), and the direction of twinning shear is rational ($\langle 011 \rangle$ in this case).

Appendix B. Atomic Structure on the coherent $\{111\}$ terrace of the TB

Much of what follows is intended as a background, explained in only as much detail as required for this study. These aspects have been addressed more comprehensively in [73] where the main focus is to understand the structure of the $\langle 011 \rangle$ type II TB in B19'NiTi martensite. The crystallography of the twin variants are given in [57,59]. For atomic registry to exist between $(\bar{1}\bar{1}\bar{1})_A$ and $(11\bar{1})_B$, the crystallographic directions on the planes must align. If the common $\langle 011 \rangle$ directions of both variants are presumed to be aligned, then there is a misalignment between $[\bar{2}\bar{1}\bar{1}]_A$ and $[2\bar{1}\bar{1}]_B$ (Fig. 1B). This can be resolved by enforcing an equal and opposite shear strain of magnitude $\approx 0.96\%$ to each variant ($\gamma = \gamma_A = 0.96\%$ and $\gamma_B = -0.96\%$). Hence, a coherence strain of pure shear nature is required for atomic registry at the interface, given by:

$$\epsilon_{coh} = \begin{pmatrix} 0 & \gamma/2 & 0 \\ \gamma/2 & 0 & 0 \\ 0 & 0 & 0 \end{pmatrix} \quad (14)$$

After enforcing the coherence strains, variant structures are to be positioned over each other to form the twinned configuration of the

TB terraces. Since the structures are complicated and involve lattice and motif positions whose arrangement is unique in each variant, there can be no crystallographic TB. In other words, there is no plane of atoms which can conform to atomic arrangements in both variants. Consequently, the issue of lattice offset [82] must be addressed, determining the position of variant A relative to variant B. To define the offset, an origin is set. Consider the virtual extension of variant B's structure beyond the TB into variant A. One of the lattice sites (lattice Ti positions) on the virtual plane immediately after the TB is chosen as the origin, O_B . The position of an arbitrarily chosen lattice site in variant A (labeled O_A) on the prospective adjacent plane to the TB, with reference to this chosen origin, defines the offset vector (x_0, y_0, z_0) (shown in Fig. 2B (i, ii)). Here the axes are chosen such that $x \parallel [011], y \parallel [\bar{2}\bar{1}\bar{1}]_A, z \parallel n_{\{111\}}$. The normalized counterparts ($\bar{x}_0 = x_0/[011], \bar{y}_0 = y_0/[\bar{2}\bar{1}\bar{1}]_A, \bar{z}_0 = z_0/n_{\{111\}}$) shall be used. The HRTEM study [57] clarifies the offsets to a major extent by specifying that the variants look identical when viewed along $\langle 011 \rangle$. This narrows down the admissible offsets to $\bar{z}_0 = 0.048$ and $\bar{y}_0 = 0.128, 0.628$. To determine \bar{x}_0 , an iterative relaxation procedure is carried out within MS. The atomistic procedure similar to that employed for “isosceles” twin boundaries [83] is utilized.

Twinned configurations at various $0 \leq \bar{x}_0 < 1$ values are constructed inside a simulation box with the axes aligned in the manner mentioned before. Since x and y axes are aligned along crystallographic directions, periodic conditions are enforced along them to simulate a bulk material, while the non-crystallographic z direction is shrink-wrapped. A layer of atoms, 6 \AA^0 thick is frozen at the top and bottom boundaries (ends of the z span of the simulation box) representative of the unperturbed atomic structure far from the TB. The thickness is chosen to be higher than the interatomic potential's cut-off ($r_c = 5.2 \text{ \AA}^0$) [40]. Now, for each \bar{x}_0 , this setup is subjected to an energy minimization routine in LAMMPS utilizing the conjugate gradient method. The simulation box sizes along the periodic axes is allowed to relax using the box/relax command to allow a dilatational relaxation of the twin configuration, further lowering the energy. The convergence tolerance is set at a fractional energy change of 1.0×10^{-8} . This minimization is carried out at each \bar{x}_0 , in the range $0 \leq \bar{x}_0 < 1$. Steps of 0.01 are chosen. And this complete iteration is repeated for both the candidate offsets $\bar{y}_0 = 0.128, 0.628$, and a fixed $\bar{z}_0 = 0.048$. The offsets are specified as an “origin” parameter in LAMMPS (used when defining the lattices in the code). The results are presented in Fig. 2B (iii), where the offset combination $\bar{y}_0 = 0.128, \bar{x}_0 = 0.522$ or $\bar{y}_0 = 0.628, \bar{x}_0 = 0.022$ provides the minimum energy configuration. It turns out that both these combinations are crystallographically equivalent and result in the same TB structure. Now the twin segment can be setup with both the variants positioned across

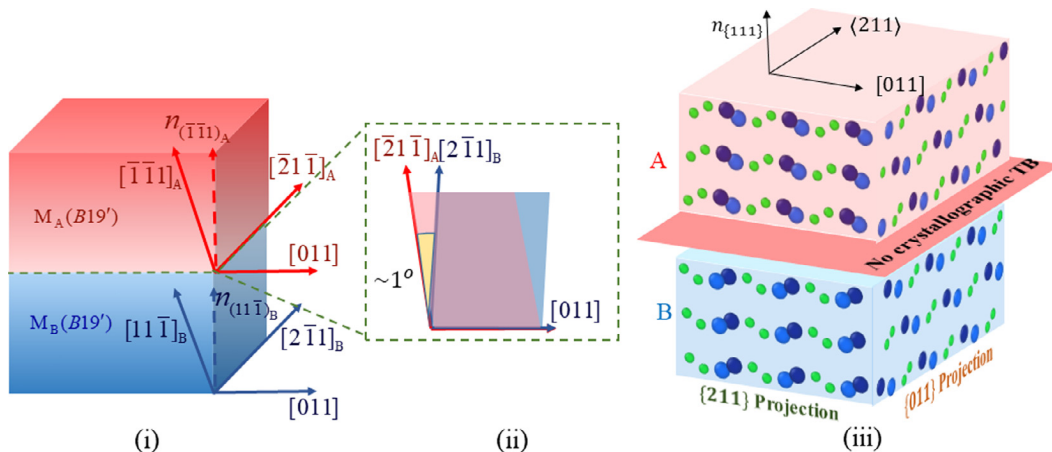


Fig. 1B. (i) Crystallography of the martensitic twin variants indicating (ii) the in-plane shear mismatch (iii) Projections of the twin variant structures shown in a 3D form illustrating that no crystallographic TB is possible accommodating the unique atomic arrangements in both variants.

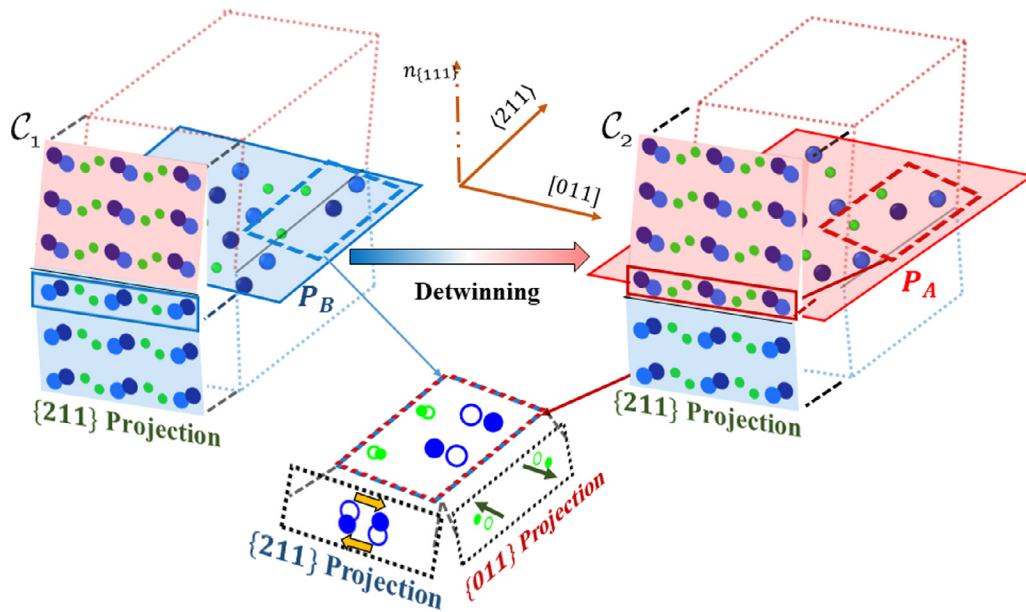


Fig. 1C. Comparison of two coherent $\{111\}$ twin segments C_1 and C_2 : $\{211\}$ projections of the segments are shown with 3D views of crystallographic planes P_A and P_B (the atomic arrangement in P_B detwins to that in P_A); an overlap of aptly chosen repeating units in both planes establishes the necessary atomic motions for detwinning.

the TB at a relative offset of $(\bar{x}_0 = 0.522, \bar{y}_0 = 0.1285, \bar{z}_0 = 0.048)$ or $(\bar{x}_0 = 0.022, \bar{y}_0 = 0.628, \bar{z}_0 = 0.048)$, the offset being specified using the “origin” parameter in LAMMPS.

Appendix C. Atomic shuffles for detwinning

In this section, the atomic motions necessary for detwinning are established. Subsequently, their connection with the twinning partial magnitude is established through a simulation of the Generalized Planar Fault Energy (GPFE) curve. The first step involves asserting the required motions from an analysis of the variant structures, independent of any atomistic simulation. For this purpose, two coherent $\{111\}$ twin segments, C_1 and C_2 , are constructed that only differ in the relative position of the TB (Fig. 1C). In C_2 , the TB has migrated one layer plane into variant B. A comparison of a repeating unit in the crystallographic planes P_B (variant B in C_1) and P_A (variant A in C_2) establishes the necessary detwinning atomic motions. Again, a more detailed description is provided in [73]. For this study, it suffices to say that the Ti atoms undergo “interchanging” shuffles along $[011]$, while the Ni atoms undergo $\{211\}$ and $n_{\{111\}}$ shuffles (refer Fig. 1C). The “interchanging” is used to imply the lattice-motif Ti shuffle, where the lattice Ti of variant B shuffles to a motif Ti position in variant A and vice versa. The usefulness of the choice in labeling atomic sites in Section 2.1 is realized here, where this shuffle is simply put as an exchange in the position of the dark-blue and light-blue spheres representing these atomic sites. A similar labeling with Ni atoms would have made their shuffles distinctive as well, but they were omitted for the sake of brevity in the figures of this study, avoiding an over-complicated picture. Note that the detwinning mechanism is dominantly shuffle-reliant close to the TB.

Appendix D. GPFE curve for $\langle 011 \rangle$ Type II TB

The detwinning mechanism established in Appendix C is realized within a MS framework by simulating the twin migration segment of the GPFE curve for this twinning mode. An earlier *ab initio* study on the energetics of this twinning mode already established the complete GPFE curve [59]. In this study, the GPFE simulation has implications to the incorporation of twinning partials within an atomistic framework,

particularly to the manner in which continuum displacement fields will be applied around the twinning partial cores, in Section 2.2.2. Since this is not outlined in [59], the simulation is repeated with this separate focus in a different framework (MS) than that study. Given that the MS simulation relies on an empirical interatomic potential that was not fit to any twinning energy signature, the energetics aren't as accurate. Still, it has sufficient capability for the specified purpose and is a more practical alternative because the consequent utility in atomistic incorporation of twin partials cannot be realized in *ab initio* frameworks (similar to that used in [59]) without incurring high computational costs. The GPFE calculation has a standard procedure [41] and has been widely used in estimating detwinning energy barriers [42,77,80]. For the twin migration segment, the standard procedure involves a rigid translation of one twin variant over the other twin variant. Rigid displacements are enforced to all atoms of the mobile variant. The potential energy of the system is tracked at each incremental displacement while shuffles are selectively allowed normal to the direction of displacement. An illustration is shown in Fig. 1D(i), modeled after FCC systems [84]. Typically in such high-symmetry systems the TB is also crystallographic [32,33] and is translated along with the top variant. In fact, in cubic systems the twinning is *only of the compound type* [85] and the TB is consequently a rational crystallographic atomic plane. Hence, a GPFE calculation only requires introduction of translational disregistry at the TB with minor role of atomic shuffles. This procedure migrates the TB by one plane and the tracked energy traces the contour termed as the GPFE twin migration segment. If the same procedure were to be repeated for $B19'$ NiTi say to switch from configuration C_1 to C_2 (Fig. 1D(ii)), a rigid $[011]$ displacement applied to all atoms of variant A cannot migrate the TB. This is because the procedure does not admit the (dominantly) shuffle-reliant mechanism at the TB. Also, there is no crystallographic TB in this case, and the translating variant A cannot account for shuffles in the variant B plane which is to prospectively detwin. Particularly in this case, shuffles anti-parallel to the direction of the enforced displacement ($[011]$ Ti shuffles outlined before) must be accounted for.

To achieve these shuffles, the rigid displacements must be applied more selectively. The rigid displacement is enforced along $[011]$ only on lattice Ti sites of variant A, and lattice Ti sites of the variant B plane which is to prospectively detwin (Fig. 2D). The remaining Ti and Ni

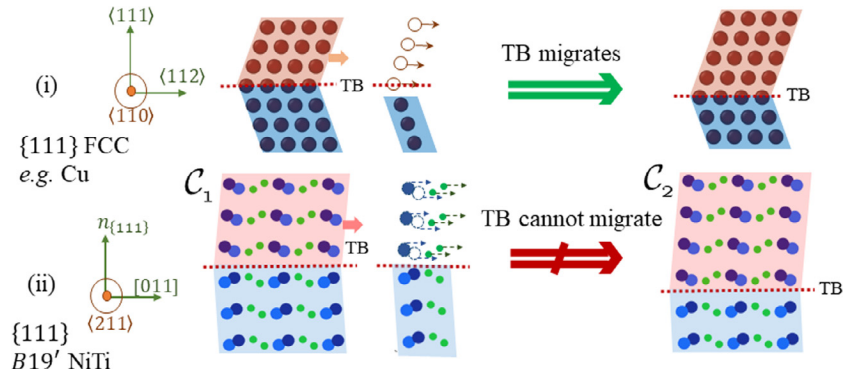


Fig. 1D. Illustrating the procedure for calculation of the GPFE twin migration segment: (i) In systems of higher symmetry such as cubic FCC, the twin migrates through a rigid translation enforced on all atoms of one variant (and the TB) whereas (ii) the same procedure cannot apply to migrate the TB in a low-symmetry phase such as B19' martensite; shuffles must be admitted.

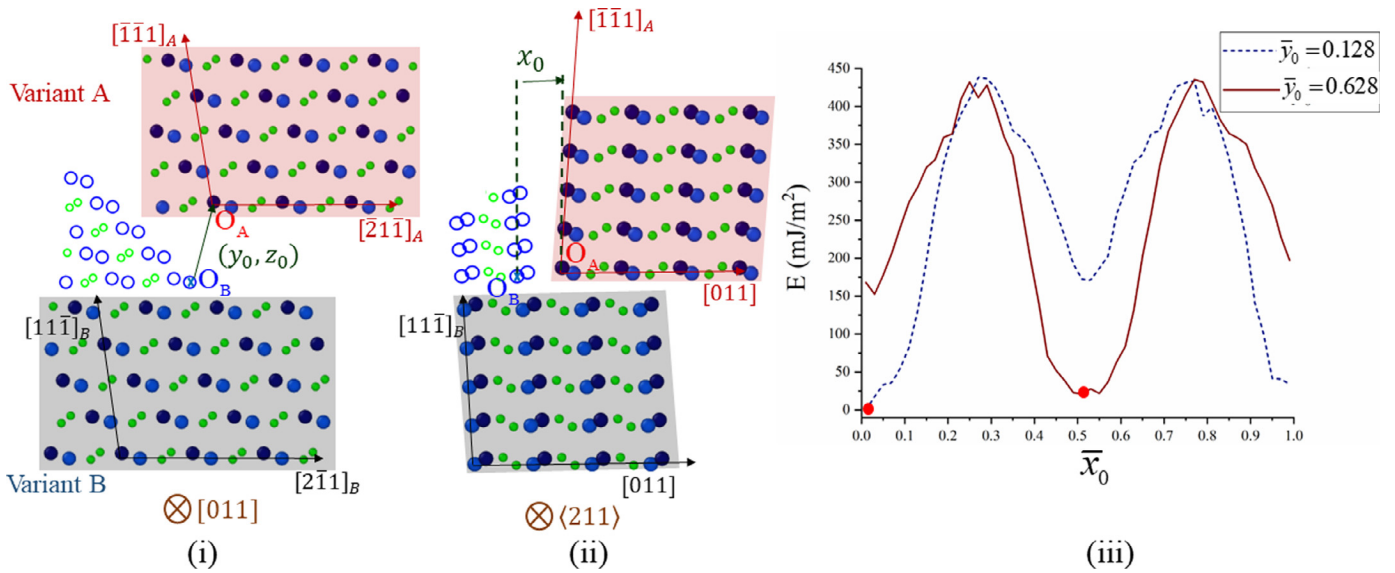


Fig. 2B. (i) Offsets (y_0, z_0) illustrated on the $[011]$ projections of the twin variants, between the chosen origins; the open circles represent a virtual extension variant B atomic positions beyond the TB (used as a reference to define the lattice offset) (ii) Offset x_0 illustrated on the $[211]$ projection, varied incrementally in the MS simulation setup (iii) Results of the MS simulation determining the offset position corresponding to the minimum energy (thereby completing the description of the twin structure).

sites on these corresponding planes are allowed to shuffle without constraint, thereby admitting the required shuffles asserted in the preceding crystallographic analysis. These are implemented within an MS simulation. The twin segment C_1 is constructed in MS with boundary conditions similar to those outlined in Section 2.1. At each incremental displacement, and with the mentioned constraints, energy is minimized using the conjugate gradient method in LAMMPS, with a convergence tolerance of 1.0×10^{-8} . The results are shown in Fig. 2D.

The enforced displacements are normalized against the formerly known twinning partial magnitude [59]. In this study, the magnitude is slightly lower around $b' \approx 0.7b$, where $b = 1/9[011]$. There are discrepancies in the GPFE curve such as the higher energy barrier and a more unsymmetric appearance than in [59]. Also, while the lattice-motif Ti shuffles are achieved, the Ni shuffles are only partially achieved. Nevertheless these are due to the limited capabilities of the governing potential, but it serves the purpose of this study and it doesn't affect the physics in the simulation of the dislocation reaction.

An important consequence of the distinction between the high-symmetry FCC example and the low-symmetry martensite case is worth noting here. If the rigid displacement of the GPFE calculation is treated analogous to an applied twinning shear, then it is observed that certain atoms follow the applied twinning shear while others

shuffle about them, not conforming to the applied shear. In the martensite phase, the specific lattice Ti sites conform to the shear whereas the remaining atoms are at the mercy of the potential. Closer to the TB, there is a higher propensity for shuffles (particularly against the direction of the applied shear) thereby not adhering to the Cauchy-Born assumption. Whereas further away from the TB, for instance closer to the top and bottom extremities, all atoms move along the shear with less/no shuffles showing higher propensity to follow the Cauchy-Born assumption. It is the magnitude of the displacement at these extremities that corresponds to the twinning partial magnitude. In contrast, for the high-symmetry structure, all atoms tend to follow the assumption and no such gradation in behavior is observed closer/away from the interface. This has a very important bearing in creation of twinning partial within the MS framework as is elaborated in Section 2.2.2.

The authors have attempted to provide a succinct description sufficiently complete to continue with the proposed study. A more detailed description can be found in [73] where the main focus is in explaining the structure and twin migration mechanism for the TB. Further, several aspects such as equal partitioning of coherence strain (between variants), significance of coherence strain in explaining TB geometry, significance of lattice offset to detwinning mechanism etc. are addressed there to provide a more holistic coverage of TB structure.

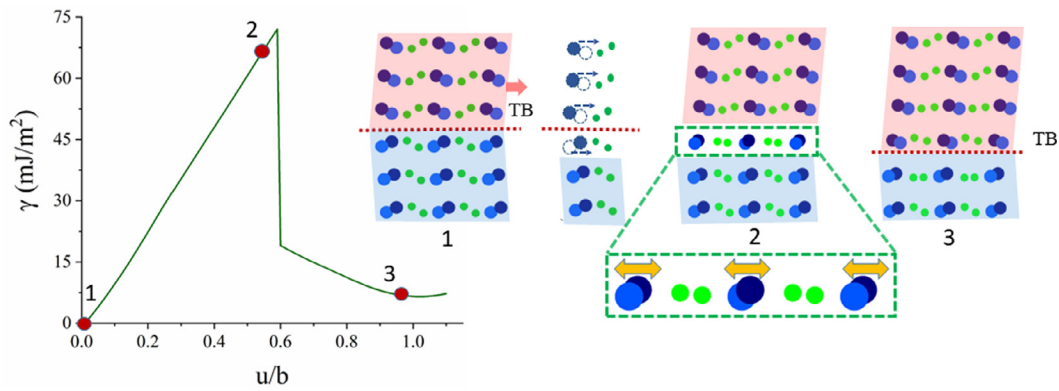


Fig. 2D. MS calculation of GPFE twin migration segment for (011) type II twin terrace in NiTi martensite; the rigid displacements are selectively enforced on specific Ti sites to simulate the shuffle-dominant detwinning mechanism at the TB.

References

- [1] K. Otsuka, C.M. Wayman, *Shape Memory Materials*, University press, Cambridge, 1999.
- [2] H. Sehitoglu, et al., Compressive response of NiTi single crystals, *Acta Mater* 48 (13) (2000) 3311–3326 2000/08/01/.
- [3] K.N. Melton, O. Mercier, Fatigue of NiTi thermoelastic martensites, *Acta Metallurgica* 27 (1) (1979) 137–144 1979/01/01/.
- [4] G. Eggeler, E. Hornbogen, A. Yawny, A. Heckmann, M. Wagner, Structural and functional fatigue of NiTi shape memory alloys, *Mater. Sci. Eng. A* 378 (1) (2004) 24–33 2004/07/25/.
- [5] P. Chowdhury, H. Sehitoglu, A revisit to atomistic rationale for slip in shape memory alloys, *Prog. Mater. Sci.* 85 (2017) 1–42 2017/04/01/.
- [6] P. Chowdhury, H. Sehitoglu, Deformation physics of shape memory alloys – Fundamentals at atomistic frontier, *Prog. Mater. Sci.* 88 (2017) 49–88 2017/07/01/.
- [7] S. Kajiware, W.S. Owen, Substructure of austenite formed by a partial reverse martensitic transformation in an Fe-ppt alloy, *Metallurg. Trans.* 4 (8) (1973) 1988–1990 1973/08/01/.
- [8] S. Kajiware, T. Kikuchi, Dislocation structures produced by reverse martensitic transformation in a Cu-Zn alloy, *Acta Metallurg.* 30 (2) (1982) 589–598 1982/02/01/.
- [9] M. Sade, R. Rapacioli, M. Ahlers, Fatigue in Cu-Zn-Al single crystals, *Acta Metallurg.* 33 (3) (1985) 487–497 1985/03/01/.
- [10] X. Jiang, M. Hida, Y. Takemoto, A. Sakakibara, H. Yasuda, H. Mori, *In situ* observation of stress-induced martensitic transformation and plastic deformation in TiNi alloy, *Mater. Sci. Eng. A* 238 (2) (1997) 303–308 1997/11/15/.
- [11] C. Damiani, M. Sade, F.C. Lovey, Fatigue in Cu-Zn-Al single crystals during pseudoelastic cycling: *in situ* observations by SEM and optical microscopy, *J. Phys. IV France* 112 (2003) 623–626 10.1051/jp4:200396210/.
- [12] D.M. Norfleet, et al., Transformation-induced plasticity during pseudoelastic deformation in Ni-Ti microcrystals, *Acta Mater* 57 (12) (2009) 3549–3561 2009/07/01/.
- [13] T. Simon, A. Kröger, C. Somsen, A. Dlouhy, G. Eggeler, On the multiplication of dislocations during martensitic transformations in NiTi shape memory alloys, *Acta Mater* 58 (5) (2010) 1850–1860 2010/03/01/.
- [14] R. Delville, B. Malard, J. Pilch, P. Sittner, D. Schryvers, Transmission electron microscopy investigation of dislocation slip during superelastic cycling of Ni-Ti wires, *Int. J. Plastic.* 27 (2) (2011) 282–297 2011/02/01/.
- [15] A.R. Pelton, G.H. Huang, P. Moine, R. Sinclair, Effects of thermal cycling on microstructure and properties in nitinol, *Mater. Sci. Eng. A* 532 (2012) 130–138 2012/01/15/.
- [16] R.F. Hamilton, H. Sehitoglu, Y. Chumlyakov, H.J. Maier, Stress dependence of the hysteresis in single crystal NiTi alloys, *Acta Mater* 52 (11) (2004) 3383–3402 2004/06/21/.
- [17] M.F.X. Wagner, N. Nayan, U. Ramamurty, Healing of fatigue damage in NiTi shape memory alloys, *J. Phys. D Appl. Phys.* 41 (18) (2008) 185408 2008/08/28/.
- [18] C. Maletta, E. Sgambitterra, F. Furguiele, R. Casati, A. Tuissi, Fatigue of pseudoelastic NiTi within the stress-induced transformation regime: a modified Coffin–Manson approach, *Smart Mater. Struct.* 21 (11) (2012) 112001 2012/09/14/.
- [19] C. Maletta, E. Sgambitterra, F. Furguiele, R. Casati, A. Tuissi, Fatigue properties of a pseudoelastic NiTi alloy: strain ratcheting and hysteresis under cyclic tensile loading, *Int. J. Fatigue* 66 (2014) 78–85 2014/09/01/.
- [20] W. Abuzaid, H. Sehitoglu, Functional fatigue of Ni50.3Ti25Hf24.7 – Heterogeneities and evolution of local transformation strains, *Mater. Sci. Eng. A* 696 (2017) 482–492 2017/06/01/.
- [21] W. Abuzaid, H. Sehitoglu, Superelasticity and functional fatigue of single crystal-line FeNiCoTi iron-based shape memory alloy, *Mater Des* 160 (2018) 642–651 2018/12/15/.
- [22] J.M. Young, K.J. Van Vliet, Predicting *in vivo* failure of pseudoelastic NiTi devices under low cycle, high amplitude fatigue, *J. Biomed. Mater. Res. Part B Appl. Biomater.* 72B (1) (2005) 17–26 2005/01/15/.
- [23] J. Zhang, et al., Leaf-like dislocation substructures and the decrease of martensitic start temperatures: a new explanation for functional fatigue during thermally induced martensitic transformations in coarse-grained Ni-rich Ti–Ni shape memory alloys, *Acta Mater* 60 (5) (2012) 1999–2006 2012/03/01/.
- [24] T. Ezaz, J. Wang, H. Sehitoglu, H.J. Maier, Plastic deformation of NiTi shape memory alloys, *Acta Mater* 61 (1) (2013) 67–78 2013/01/01/.
- [25] R.C. Pond, S. Celotto, J.P. Hirth, A comparison of the phenomenological theory of martensitic transformations with a model based on interfacial defects, *Acta Mater* 51 (18) (2003) 5385–5398 2003/10/20/.
- [26] X. Ma, R.C. Pond, Parent–martensite interface structure in ferrous systems, *J. Nuclear Mater.* 361 (2) (2007) 313–321 2007/04/15/.
- [27] R.C. Pond, X. Ma, J.P. Hirth, T.E. Mitchell, Disconnections in simple and complex structures, *Philosoph. Mag.* 87 (33) (2007) 5289–5307 2007/11/21/.
- [28] J.M. Howe, R.C. Pond, J.P. Hirth, The role of disconnections in phase transformations, *Prog. Mater. Sci.* 54 (6) (2009) 792–838 2009/08/01/.
- [29] J.P. Hirth, J. Wang, C.N. Tomé, Disconnections and other defects associated with twin interfaces, *Prog. Mater. Sci.* 83 (2016) 417–471 2016/10/01/.
- [30] X. Ma, R.C. Pond, Martensitic interfaces and transformation crystallography in Pu–Ga alloys, *J. Mater. Sci.* 46 (12) (2011) 4236–4242 2011/06/01/.
- [31] R.C. Pond, J.P. Hirth, A. Serra, D.J. Bacon, Atomic displacements accompanying deformation twinning: shears and shuffles, *Mater. Res. Lett.* 4 (4) (2016) 185–190 2016/10/01/.
- [32] S. Mahajan, D.F. Williams, Deformation twinning in metals and alloys, *Int. Metallurg. Rev.* 18 (2) (1973) 43–61 1973/06/01/.
- [33] J.W. Christian, S. Mahajan, Deformation twinning, *Prog. Mater. Sci.* 39 (1) (1995) 1–157 1995/01/01/.
- [34] J.W. Christian, CHAPTER 20 – Deformation Twinning, in: J.W. Christian (Ed.), *The Theory of Transformations in Metals and Alloys*, Oxford, Pergamon, 2002, pp. 859–960.
- [35] J.W. Christian, Crystallographic theories, interface structures, and transformation mechanisms, *Metallurg. Mater. Trans. A* 25 (9) (1994) 1821–1839 1994/09/01/.
- [36] S. Plimpton, Fast parallel algorithms for short-range molecular dynamics, *J. Comput. Phys.* 117 (1) (1995) 1–19 1995/03/01/.
- [37] J. Hafner, Ab-initio simulations of materials using VASP: density-functional theory and beyond, *J. Comput. Chem.* 29 (13) (2008) 2044–2078 2008/10/01/.
- [38] W.S. Lai, B.X. Liu, Lattice stability of some Ni-Ti alloy phases versus their chemical composition and disordering, *J. Phys. Condensed Matter* 12 (5) (2000) L53–L60 2000/01/10/.
- [39] Y. Zhong, K. Gall, T. Zhu, Atomistic study of nanotwins in NiTi shape memory alloys, *J. Appl. Phys.* 110 (3) (2011) 033532 2011/08/01/.
- [40] G. Ren, H. Sehitoglu, Interatomic potential for the NiTi alloy and its application, *Comput. Mater. Sci.* 123 (2016) 19–25 2016/10/01/.
- [41] S. Ogata, J. Li, S. Yip, Energy landscape of deformation twinning in bcc and FCC metals, *Phys. Rev. B* 71 (22) (2005) 224102 06/09/.
- [42] P. Chowdhury, H. Sehitoglu, Atomistic energetics and critical twinning stress prediction in face and body centered cubic metals: recent progress, *J. Eng. Mater. Technol.* 140 (2) (2018) pp. 020801–020801-19.
- [43] T. Duerig, A. Pelton, D. Stöckel, An overview of nitinol medical applications, *Mater. Sci. Eng. A* 273–275 (1999) 149–160 1999/12/15/.
- [44] K. Otsuka, X. Ren, Physical metallurgy of Ti–Ni-based shape memory alloys, *Prog. Mater. Sci.* 50 (5) (2005) 511–678 2005/07/01/.
- [45] H. Tobushi, T. Hachisuka, S. Yamada, P.-H. Lin, Rotating-bending fatigue of a TiNi shape-memory alloy wire, *Mech. Mater.* 26 (1) (1997) 35–42 1997/07/01/.
- [46] H. Tobushi, T. Hachisuka, T. Hashimoto, S. Yamada, Cyclic deformation and fatigue of a TiNi shape-memory alloy wire subjected to rotating bending, *J. Eng. Mater. Technol.* 120 (1) (1998) 64–70.
- [47] S. Miyazaki, K. Mizukoshi, T. Ueki, T. Sakuma, Y. Liu, Fatigue life of Ti–50 at.% Ni and Ti–40Ni–10Cu (at.%) shape memory alloy wires, *Mater. Sci. Eng. A* 273–275 (1999) 658–663 1999/12/15/.
- [48] D.C. Lagoudas, D.A. Miller, L. Rong, P.K. Kumar, Thermomechanical fatigue of shape memory alloys, *Smart Mater. Struct.* 18 (8) (2009) 085021 2009/07/01/.

- [49] S.W. Robertson, A.R. Pelton, R.O. Ritchie, Mechanical fatigue and fracture of nitinol, *Int. Mater. Rev.* 57 (1) (2012) 1–37 2012/01/01.
- [50] P. Chowdhury, G. Ren, H. Sehitoglu, NiTi superelasticity via atomistic simulations, *Philos. Mag. Lett.* 95 (12) (2015) 574–586 2015/12/02.
- [51] D. Farkas, D. Roqueta, A. Vilette, K. Ternes, Atomistic simulations in ternary ni - Ti - al alloys, *Modell. Simulat. Mater. Sci. Eng.* 4 (4) (1996) 359–369 1996/07/01.
- [52] H. Ishida, Y. Hiwatari, MD simulation of martensitic transformations in tni alloys with meam, *Mol Simul* 33 (4–5) (2007) 459–461 2007/04/01.
- [53] D. Mutter, P. Nielaba, Simulation of structural phase transitions in NiTi, *Phys. Rev. B* 82 (22) (2010) 224201 12/01/.
- [54] W.-S. Ko, B. Grabowski, J. Neugebauer, Development and application of a ni-ti interatomic potential with high predictive accuracy of the martensitic phase transition, *Phys. Rev. B* 92 (13) (2015) 134107 10/14/.
- [55] M. Muralles, S.-D. Park, S.Y. Kim, B. Lee, Phase transformations, detwinning and superelasticity of shape-memory NiTi from meam with practical capability, *Comput. Mater. Sci.* 130 (2017) 138–143 2017/04/01/.
- [56] K.M. Knowles, D.A. Smith, The crystallography of the martensitic transformation in equiatomic nickel-titanium, *Acta Metall.* 29 (1) (1981) 101–110 1981/01/01/.
- [57] Y. Liu, Z.L. Xie, Twinning and detwinning of <0 1 1> type ii twin in shape memory alloy, *Acta Mater* 51 (18) (2003) 5529–5543 2003/10/20/.
- [58] Z.L. Xie*, Y. Liu, HRTEM study of (011) type ii twin in NiTi shape memory alloy, *Philosoph. Mag.* 84 (32) (2004) 3497–3507 2004/11/11.
- [59] T. Ezaz, H. Sehitoglu, Type ii detwinning in NiTi, *Appl. Phys. Lett.* 98 (14) (2011) 141906 2011/04/04.
- [60] M.D. Sangid, H.J. Maier, H. Sehitoglu, A physically based fatigue model for prediction of crack initiation from persistent slip bands in polycrystals, *Acta Mater* 59 (1) (2011) 328–341 2011/01/01/.
- [61] D.M. Barnett, J. Lothe, An image force theorem for dislocations in anisotropic bicrystals, *J. Phys. F Metal Phys.* 4 (10) (1974) 1618–1635 1974/10/.
- [62] Y. Kudoh, M. Tokonami, S. Miyazaki, K. Otsuka, Crystal structure of the martensite in ti-49.2 at.%Ni alloy analyzed by the single crystal X-ray diffraction method, *Acta Metall.* 33 (11) (1985) 2049–2056 1985/11/01/.
- [63] G.B. Olson, M. Cohen, Interphase-boundary dislocations and the concept of coherency, *Acta Metall.* 27 (12) (1979) 1907–1918 1979/12/01/.
- [64] V. Bulatov, W. Cai, *Computer Simulations of Dislocations*, Oxford University Press, 2006.
- [65] J. Chang, W. Cai, V.V. Bulatov, S. Yip, Dislocation motion in bcc metals by molecular dynamics, *Mater. Sci. Eng. A* 309–310 (2001) 160–163 2001/07/15/.
- [66] J. Chang, W. Cai, V.V. Bulatov, S. Yip, Molecular dynamics simulations of motion of edge and screw dislocations in a metal, *Comput. Mater. Sci.* 23 (1) (2002) 111–115 2002/04/01/.
- [67] J.A. Moriarty, V. Vitek, V.V. Bulatov, S. Yip, Atomistic simulations of dislocations and defects, *J. Comput. Aided Mater. Des.* 9 (2) (2002) 99–132 2002/05/01.
- [68] X. Liu, S.I. Golubov, C.H. Woo, H. Huang, Glide of edge dislocations in tungsten and molybdenum, *Mater. Sci. Eng. A* 365 (1) (2004) 96–100 2004/01/25/.
- [69] G. Lasko, D. Saraev, S. Schmauder, P. Kizler, Atomic-scale simulations of the interaction between a moving dislocation and a bcc/fcc phase boundary, *Comput. Mater. Sci.* 32 (3) (2005) 418–425 2005/03/01/.
- [70] S. Groh, E.B. Marin, M.F. Horstemeyer, D.J. Bammann, Dislocation motion in magnesium: a study by molecular statics and molecular dynamics, *Modell. Simulat. Mater. Sci. Eng.* 17 (7) (2009) 075009 2009/08/14.
- [71] A.S. Argon, *Kinematics and kinetics in crystal plasticity, Strengthening Mechanisms in Crystal Plasticity*, Oxford University Press, Oxford, 2007.
- [72] A. Stukowski, Visualization and analysis of atomistic simulation data with OVITO—the open visualization tool, *Modelling and Simulation in Materials Science and Engineering* 18 (1) (2009) 015012 2009/12/15.
- [73] A.S.K. Mohammed, H. Sehitoglu, Martensitic Twin Boundary Migration as a Source of Irreversible Slip in Shape Memory Alloys, Manuscript Submitted for Publication, 2019.
- [74] A.W. Sleswyk, Emissary dislocations: theory and experiments on the propagation of deformation twins in α -iron, *Acta Metallurgica* 10 (8) (1962) 705–725 1962/08/01/.
- [75] R.C. Pond, X. Ma, Y.W. Chai, J.P. Hirth, Chapter 74 topological modelling of martensitic transformations, in: F.R.N. Nabarro, J.P. Hirth (Eds.), *Dislocations in Solids*, 13, Elsevier, 2007, pp. 225–261.
- [76] V. Vitek, Intrinsic stacking faults in body-centred cubic crystals, *Philosoph. Mag. A J. Theoret. Exper. Appl. Phys.* 18 (154) (1968) 773–786 1968/10/01.
- [77] A. Ojha, H. Sehitoglu, Critical stresses for twinning, slip, and transformation in ti-based shape memory alloys, *Shape Memory Superelast.* 2 (2) (2016) 180–195 2016/06/01.
- [78] S. Alkan, H. Sehitoglu, Plastic flow resistance of niticu shape memory alloy-theory and experiments, *Acta Mater* 163 (2019) 173–188 2019/01/15/.
- [79] V. Vitek, Multilayer stacking faults and twins on {211} planes in B.C.C. metals, *Scripta Metallurg.* 4 (9) (1970) 725–732 1970/09/01/.
- [80] J. Wang, H. Sehitoglu, Twinning stress in shape memory alloys: theory and experiments, *Acta Mater* 61 (18) (2013) 6790–6801 2013/10/01/.
- [81] A. Bilby Bruce, A.G. Crocker, H. Cottrell Alan, The theory of the crystallography of deformation twinning, *Proc. R. Soc. Lond. Ser. A. Math. Phys. Sci.* 288 (1413) (1965) 240–255 1965/10/26.
- [82] R. Schweinfest, F. Ernst, T. Wagner, M. Rühle, High-precision assessment of interface lattice offset by quantitative hrem. (in eng) *J. Microsc.* 194 (1) (1999) 142–151 1999/04/.
- [83] P.D. Bristowe, A.G. Crocker, A computer simulation study of the structures of twin boundaries in body-centred cubic crystals, *Philosoph. Mag. A J. Theoret. Exper. Appl. Phys.* 31 (3) (1975) 503–517 1975/03/01.
- [84] S. Kibey, J.B. Liu, D.D. Johnson, H. Sehitoglu, Generalized planar fault energies and twinning in cu–al alloys, *Appl. Phys. Lett.* 89 (19) (2006) 191911 2006/11/06.
- [85] A. Kelly, K.M. Knowles, Chapter 11 - Twinning, *Crystallography and Crystal Defects*, John Wiley & Sons Ltd., Chichester, UK, 2012, pp. 335–361.